Department of Radio Science and Engineering

Dispersion of dielectric composites: quasi-dynamic characterizations and applications

Jiaran Qi

Aalto University

DOCTORAL DISSERTATIONS

Aalto University publication series
DOCTORAL DISSERTATIONS 61/2011

Dispersion of dielectric composites: quasi-dynamic characterizations and applications

Jiaran Qi

Doctoral dissertation for the degree of Doctor of Science in Technology to be presented with due permission of the School of Electrical Engineering for public examination and debate in Auditorium S4 at the Aalto University School of Electrical Engineering (Espoo, Finland) on the 14th of September 2011 at 13 o'clock.

Aalto University
School of Electrical Engineering
Department of Radio Science and Engineering
Electromagnetics

Supervisor
Professor Ari Sihvola

Instructor
Professor Ari Sihvola

Preliminary examiners
Professor Christian Mätzler, University of Bern, Switzerland
Associate Professor Xudong Chen, National University of Singapore, Singapore

Opponent
Professor Raj Mittra, The Pennsylvania State University, USA

Aalto University publication series
DOCTORAL DISSERTATIONS 61/2011

ISBN 978-952-60-4211-4 (pdf)
ISBN 978-952-60-4210-7 (printed)
ISSN-L 1799-4934
ISSN 1799-4942 (pdf)
ISSN 1799-4934 (printed)

Aalto Print
Helsinki 2011

Finland

The dissertation can be read at http://lib.tkk.fi/Diss/

Publication orders (printed book):
julkaisut@aalto.fi

Aalto University

Abstract

Aalto University, P.O. Box 11000, FI-00076 Aalto www.aalto.fi

Author
Jiaran Qi

Name of the doctoral dissertation
Dispersion of dielectric composites: quasi-dynamic characterizations and applications

Publisher School of Electrical Engineering

Unit Department of Radio Science and Engineering

Series Aalto University publication series DOCTORAL DISSERTATIONS 61/2011

Field of research Electromagnetics

Manuscript submitted 7 April 2011 **Manuscript revised** 13 June 2011

Date of the defence 14 September 2011 **Language** English

☐ **Monograph** ☒ **Article dissertation (summary + original articles)**

Abstract

Characterization of the dispersion of macroscopic electromagnetic properties of composite materials is a challenging task, but it offers an efficient and effective path to interpret features or phenomena, and to design artificial structures with desired properties. In this thesis, the quasi-dynamic homogenization is performed to characterize the dispersive electric properties of a class of dielectric composites. Although their geometry configurations are very simple, many fundamental yet significant features as well as problems appear during the quasi-dynamic homogenization process, and are thus studied in detail. The quasi-dynamic region is defined to include the quasi-static one and the frequency range close to the quasi-static limit. This thesis focuses on various homogenization models and techniques. In addition, the homogenization results by the proposed techniques are applied to explore several significant homogenization-related problems, such as quantification of the quasi-static limit, evaluation of a homogenization model, as well as the temporal pulse dynamics in dielectric (composite) materials.

Keywords homogenization, dispersion, permittivity, S-parameter retrieval, angular dispersion, Lord Rayleigh formula, quasi-static and quasi-dynamic.

ISBN (printed) 978-952-60-4210-7 **ISBN (pdf)** 978-952-60-4211-4

ISSN-L 1799-4934 **ISSN (printed)** 1799-4934 **ISSN (pdf)** 1799-4942

Location of publisher Espoo **Location of printing** Helsinki **Year** 2011

Pages 148 **The dissertation can be read at** http://lib.tkk.fi/Diss/

Preface

This thesis summarizes the studies carried out in Department of Radio Science and Engineering at Aalto University School of Electrical Engineering, under the supervision of Prof. Ari Sihvola. I wish to express my gratitude to him for giving me the opportunity to work on this topic for my thesis, and also for his guidance throughout these years. Special thanks should go to my colleagues Henrik Wallén and Henrik Kettunen for their help in the co-operative works. I am grateful to Katrina Nykänen and other supporting staff in our department. I would like to thank the pre-examiners of this thesis Prof. Christian Mätzler and Assoc. Prof. Xudong Chen for their thorough examinations as well as constructive comments. The Electronics, Communications and Automation Faculty Graduate School in Aalto University and Academy of Finland are cordially thanked for the financial supports.

Finally, I wish to express my sincere gratitude to my father Guojun Qi, my mother Lianying Zhang, my father-in-law Xiaobin Li, my mother-in-law Shuzhen Li and my dear wife Li Li.

Otaniemi, June 2011 Jiaran Qi (祁嘉然)

Contents

List of publications

[P1] Jiaran Qi and Ari Sihvola, "Dispersion of the dielectric Fröhlich model and mixtures," *IEEE Transactions on Dielectrics and Electrical Insulation*, vol. 18, pp. 149–154, 2011.

[P2] Jiaran Qi, Henrik Kettunen, Henrik Wallén and Ari Sihvola, "Quasi-dynamic homogenization of geometrically simple dielectric composites," *Applied Computational Electromagnetics Society Journal*, vol. 25, pp. 1036–1045, 2010.

[P3] Henrik Kettunen, Jiaran Qi, Henrik Wallén and Ari Sihvola, "Homogenization of thin dielectric composite slabs: techniques and limitations," *Applied Computational Electromagnetics Society Journal*, vol. 26, pp. 179–187, 2011.

[P4] Jiaran Qi, Henrik Kettunen, Henrik Wallén and Ari Sihvola, "Compensation of Fabry–Pérot resonances in homogenization of dielectric composites," *IEEE Antennas and Wireless Propagation Letters*, vol. 9, pp. 1057–1060, 2010.

[P5] Jiaran Qi, Henrik Kettunen, Henrik Wallén and Ari Sihvola, "Different homogenization methods based on scattering parameters of dielectric-composite slabs," *Radio Science*, in press (available at: www.agu.org/journals/rs/papersinpress.shtml)

[P6] Jiaran Qi and Ari Sihvola, "Truncation effect on precursor field structure of pulse propagation in dispersive media," *Progress In Electromagnetics Research B*, vol. 14, pp. 65–86, 2009.

[P7] Jiaran Qi and Ari Sihvola, "Evolution of the time-domain structure of electromagnetic pulse propagating in aqueous mixtures," *Proceedings of the 8th International Conference on Electromagnetic Wave Interaction with Water and Moist Substances*, pp. 223–230, June, 2009, Espoo, Finland.

Author's contribution

[P1] The idea of analyzing the dispersion mechanisms of the Fröhlich model and the corresponding raisin mixtures was proposed by Professor Sihvola. This author wrote the paper and derived most of the results. The DDTD and the LDDD mechanisms of the Fröhlich mixtures were developed by both authors.

[P2] The idea of this paper was formulated together by all the authors. This author wrote the paper, performed the numerical simulation to get the S-parameters and dispersion diagram ready for retrievals, wrote a MATLAB code to solve the complex root of a function with complex coefficients, and proposed the compensation method. The co-authors also provided valuable comments for the manuscript.

[P3] This work was mainly done by Henrik Kettunen. This author simulated the S-parameters from the same geometry by CST MWS to compare with the results by Comsol Multiphysics. This author also helped in preparation for the manuscript.

[P4] The idea of this paper was proposed and formulated by this author. The co-authors gave valuable comments on the manuscript.

[P5] The idea of this paper was proposed and formulated mainly by this author. The idea of developing an interpolation function for the quasi-static limit was inspired by the discussion with Professor Sihvola. The co-authors provided valuable comments for the manuscript.

[P6, P7] Both authors contributed in the formulation of the ideas of these papers. The numerical results were computed by this author.

List of abbreviations

2D	two dimensions or two dimensional
3D	three dimensions or three dimensional
A-model	anisotropic model
ABL-model	stratified model with anisotropic boundary layers
AD	angle dependent
AID	angle independent
BSCM	both-S-parameter method with compensation
CST MWS	Computer Simulation Technology, Microwave Studio
DDTD	double Debye-type dispersion
EM	electromagnetics
EWM	effective wavelength method
FEM	finite element method
FFT	fast Fourier transform
FPMM	forward propagation matrix method
FPR	Fabry–Pérot resonance
H-model	homogeneous model
IBL-model	stratified model with isotropic boundary layers
IFFT	inverse fast Fourier transform
LDDD	a combination of one Lorentz-type, one shifted passive Debye-type and one shifted active-Debye-type dispersions
LMA	Levenberg–Marquardt algorithm
MEP	model evaluation process
MG	Maxwell Garnett
NRW method	Nicolson–Ross–Weir method
PEC	perfect electric conductor
PMC	perfect magnetic conductor
S-parameters	scattering parameters
TE	transverse electric
TEM	transverse electromagnetic
TM	transverse magnetic

1. Introduction

Composites are materials whose inhomogeneities on length scale are much larger than the atomic scale [1]. If the inhomogeneity length scales are very small compared with a defined macroscopic one, the composites can be effectively treated as homogeneous materials. Homogenization of a composite may refer to an averaging mechanism to characterize some of its macroscopic properties in a less rigorous yet more efficient manner than the fully microscopic description [1–4]. In electromagnetism, homogenization is a process to describe the macroscopic electromagnetic (EM) properties of a composite, often measured by the effective permittivity ε_{eff} and the effective permeability μ_{eff}, using a presumed homogenization model.

The physical validity of a homogenization process is defined by the inhomogeneity length scales of the composites. More precisely, it depends on whether the heterogeneity of the composite can macroscopically be sensed by the impinging electromagnetic field. In order to reflect the sensitivity of the EM field to the inhomogeneities of a given composite, the frequency spectrum is qualitatively categorized in Fig. 1 according to the ratio between the inhomogeneity length scale (denoted as a) and the effective wavelength (denoted as λ_{eff}) of the EM field inside the composite.

When a/λ_{eff} is far smaller than unity, which serves as a strict condition for a physically sound homogenization, the field solutions come close to the electrostatic ones. Then, the composite can effectively be replaced by a homogeneous medium having the same macroscopic EM responses. This area is often named after 'quasi-static' or 'long-wavelength' region. However, when a/λ_{eff} is rather large, spatial dispersion causes a non-local relation between the displacement field at a point inside the composites and the electric fields around the same point [2]. This non-locality prevents a physically reasonable homogenization from being performed. A typical composite in this region would be the class of photonic crystals [5], periodic nanostructures designed to control the motion of photons. There, often the refractive index rather than ε_{eff} and μ_{eff} could be established with physical meaning. [6–8].

Between the aforementioned two conditions, there is an intermediate one when a is small but not small enough compared with λ_{eff}. Particularly, in the lower part of this intermediate region, the EM fields have relatively small variations inside the composites and the non-locality due to spatial dispersion is not very strong, so that the homogenization process could approximately be applied. As a matter of convenience, a term 'quasi-dynamic region' is defined

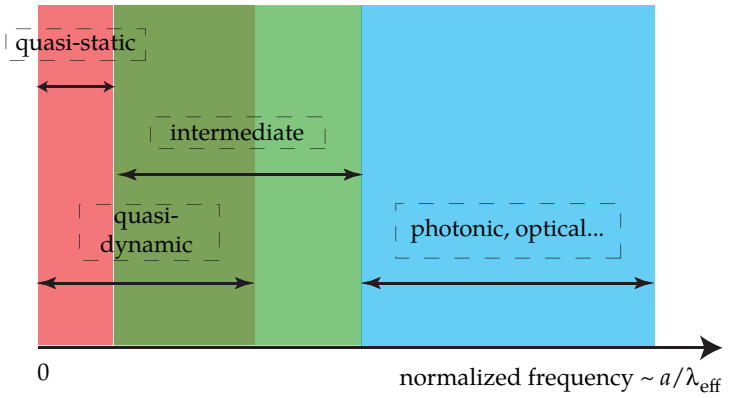

Figure 1 The frequency-spectrum classification in terms of the sensitivity of the impinging electromagnetic field to the geometric details of a given composite. The low frequency part of the quasi-dynamic region near the statics is known as the quasi-static one, or long-wavelength regime.

in this thesis to describe the frequency range that contains both the lower part of the intermediate region and the quasi-static region, as shown in Fig. 1. In this quasi-dynamic region, this thesis models the frequency dispersion of the macroscopic electrical properties of a class of dielectric composites. The composites consist of two dielectric material phases with well-established boundaries, and one phase of the composites is circular in two dimensions (2D) or spherical in three dimensions (3D).

One motivation to study the dispersion of composites is the following. In dispersion engineering, where desired dispersions are tailored by proper mixing processes, it is crucial to understand how the frequency dependence of the macroscopic medium parameters of a composite is affected by dispersions, geometries and arrangement of its constituents [9, 10]. Suppose that in the quasi-dynamic (or at least the quasi-static) region one can safely replace the real composite by an effective homogeneous medium, and the effective permittivity can be defined. For the above-mentioned dielectric composites, the classical mixing formulas can then be adopted to model its effective permittivity. In Chapter 2 and [P1], the Maxwell Garnett mixing formula [11] is applied to analyze the dependence of the dispersion mechanisms of the dielectric composites on those of their dispersive constituents.

More strictly speaking, in the quasi-dynamic region, the length scales of the composite inhomogeneities may become no longer sufficiently small compared with the effective wavelength. This fact breaks the prerequisite of the homogenization theory, and will affect its accuracy and validity. One can expect that in the quasi-dynamic region the modeled effective permittivity still has predictive power but will gradually become physically less rigorous as the frequency grows. Many artificially structured metamaterials [12–14] are typi-

cal composites in this region, whose unit cell sizes are often a fraction of the effective wavelength in their operating frequency ranges. Numerous homogenization attempts for various metamaterials have been reported, but many of the effective parameters ε_{eff} and μ_{eff} of a homogeneous-medium-based model (homogeneous model) display unphysical behaviors, such as anti-resonances and non-passive phenomena [15–19].

The following questions become parts of the main concerns in the quasi-dynamic homogenization. Firstly, the most commonly used homogeneous model might be insufficient to characterize the electrical properties of the composites, and perhaps a more complex model needs to be developed. Secondly, in a strict sense, a certain homogenization model should operate equally well when the composites are radiated by different EM sources. Finally, what could be the obstacles or problems resulting in the gradual collapse of the homogenization theory, and how to visualize them? To address these questions, one needs the corresponding homogenization methods to determine the dispersion of the effective parameters of the applied homogenization models, which are not necessarily as straightforward as the homogeneous one.

In Chapter 3 and [P2–P5], a class of geometrically simple yet feature-rich dielectric composites is considered. The quasi-dynamic homogenization methods to model their dispersive dielectric properties are then presented, including the scattering-parameter (S-parameter) retrievals, the field-averaging method, as well as the dispersion diagram method. The retrieved medium parameters are given, and the errors due to the homogenization methods are discussed. Moreover, modeling only the quasi-dynamic dielectric properties gives us freedom to choose more complex homogenization models than a homogeneous medium with ε_{eff}.

The following chapter and [P2, P5–P7] apply the homogenization results to explore some issues related to the homogenization process. A procedure to quantify the upper limiting frequency f_{L} of the quasi-static estimate based on the static Lord Rayleigh formula [20] is firstly presented for the composites introduced in Chapter 3. Furthermore, a model evaluation process (MEP) is introduced. According to the MEP, the performances of the proposed homogenization models in Chapter 3 are evaluated. Finally, the transient evolutions of Gaussian pulses propagating through the dielectric (composite) materials are analyzed by Fast Fourier Transform (FFT). Summaries of the original publications are provided in Chapter 5.

2. Mixing effects on dispersion mechanism

The frequency dispersion of the permittivity of a homogeneous material arises from its molecular and atomic structures. Relaxation dispersion and resonance dispersion are the major dielectric mechanisms [21–24]. The relaxation mechanism is typically caused by the delay in molecular polarization when a dielectric material is exposed to a varying electric field. On the other hand, ionic and electronic polarizations exhibit the resonance mechanism. Every mechanism is centered at the corresponding characteristic frequency, the reciprocal of which is the characteristic time of the process [25].

In addition to atomic and molecular polarizations, the dispersion of the effective permittivity of a dielectric composite also depends on the polarization mechanisms in the scale of its constituents. In this chapter, a class of two-phase dielectric composites is considered. The composites consist of well-separated dispersive spherical inclusions embedded in a non-dispersive background. The inclusions are assumed to follow the classical dielectric dispersions: the Debye model [26], the Lorentz model [27], and the Fröhlich model [28]. If the inclusion dimension is much smaller than the effective wavelength, the mixing formulas can be applied to analyze the effect of mixing on the dispersion mechanism, i.e., the relation between the dispersion of the composite and that of its dispersive inclusions.

2.1 Classical dielectric dispersion models

Several significant dispersion models that natural materials may display are introduced. These models, unlike real material samples, may only contain a particular dispersion mechanism. But in a limited frequency range, one of these models could reasonably describe the dispersion of a dielectric material.

2.1.1 The Debye model

The Debye model is commonly used to describe the dielectric response of liquid, especially water and dilute solutions. The Debye-type dispersion is a typical representative of the relaxation mechanism and governed by a characteristic parameter: relaxation time τ, which is often a function of temperature. The relaxation time can be perceived as the response time for the orientation

alignment of permanent dipoles to the applied constant external field. The frequency dependence of the relative permittivity predicted by the Debye model reads [29]

$$\varepsilon(\omega) = \varepsilon_\infty + \frac{\varepsilon_s - \varepsilon_\infty}{1 + j\omega\tau}, \tag{1}$$

where ε_s and ε_∞ denote the relative static and relative high-frequency permittivities of the medium. The time convention $\exp(j\omega t)$ is used throughout this thesis, except that in [P1] and [P6] the harmonic time variation $\exp(-i\omega t)$ is applied.

2.1.2 The Lorentz model

The Lorentz model [27] is of fundamental importance in solid-state physics since it offers a physically reasonable description of both normal and anomalous dispersion phenomena in a rather wide electromagnetic spectrum, from microwave to optics [30]. The Lorentz model displays a dispersion mechanism due to resonance polarization, and reads in frequency domain [29]

$$\varepsilon(\omega) = \varepsilon_\infty + \frac{\omega_p^2}{\omega_0^2 - \omega^2 + j\omega\nu}, \tag{2}$$

where the resonance frequency ω_0 measures the oscillation of charges bound elastically to an equilibrium position, and a natural material often displays multiple resonance frequencies; the plasma frequency of the medium ω_p depends only on the total number of electrons per unit volume; and the damping frequency ν characterizes the so-called phenomenological damping force [21]. In particular, when ω_0 vanishes, the Lorentz model reduces to the Drude model, which is often used to describe the optical permittivities of metals.

2.1.3 The Fröhlich model [P1]

Different from the previously introduced ones, the Fröhlich dispersion model shows a distinctive mechanism which can be considered as a transition one from the relaxation type to the resonance type when its characteristic parameters alter. The Fröhlich model is used in practice to describe the dielectric behaviors of different gases or vapors, and reads [28, 29, and 31]

$$\varepsilon(\omega) = \varepsilon_\infty + \frac{1}{2}\Delta\varepsilon\left(\frac{1 + j\omega_0\tau}{1 + j(\omega + \omega_0)\tau} + \frac{1 - j\omega_0\tau}{1 + j(\omega - \omega_0)\tau}\right), \tag{3}$$

where $\Delta\varepsilon$ is the difference between the static and high-frequency permittivites. It is clear that the Fröhlich model will reduce to the Debye one when $\omega_0\tau << 1$. With increasing $\omega_0\tau$, the resonance absorption gradually dominates over the relaxation one and contributes prevailingly to the overall power loss.

To better understand the transition mechanism of the Fröhlich dispersion, Eq. (3) can be rearranged as follows

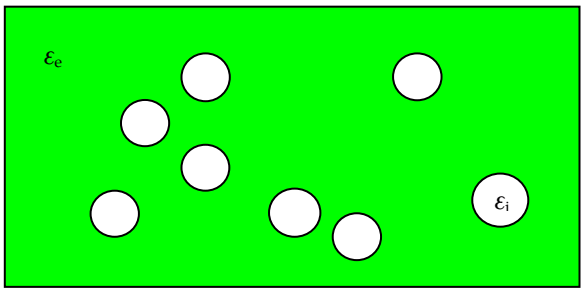

Figure 2 An illustration of the two-phase composite considered in this chapter. Spherical inclusions (ε_i) are randomly distributed in a host (background) medium (ε_e), and occupy the volume by a fraction p. Clusters of the inclusions are not allowed.

$$\varepsilon(\omega)=\underbrace{\frac{\varepsilon_\infty}{3}+\frac{1}{2}\Delta\varepsilon\underbrace{\left(\frac{1}{1+j(\omega+\omega_0)\tau}\right)}_{\text{1st}}}_{\text{Shifted passive Debye}}+\underbrace{\frac{\varepsilon_\infty}{3}+\frac{1}{2}\Delta\varepsilon\underbrace{\left(\frac{1}{1+j(\omega-\omega_0)\tau}\right)}_{\text{2nd}}}_{\text{Shifted active Debye}}$$
$$+\underbrace{\frac{\varepsilon_\infty}{3}+\frac{1}{2}\Delta\varepsilon\underbrace{\left(\frac{2\omega_0{}^2}{\omega_0{}^2+\tau^{-2}-\omega^2+j2\tau^{-1}\omega}\right)}_{\text{3rd}}}_{\text{Lorentz}}, \tag{4}$$

where the first and the second terms are two processes shifted from the Debye model by $\pm\omega_0$, and the third term represents a Lorentz-type dispersion. As $\omega_0\tau = 0$, the third term reduces to zero and the first two terms give exactly the Debye model, where only the relaxation-type dispersion is observed. When $\omega_0\tau$ increases from zero the total dispersion gradually deviates from the Debye model and is finally dominated by the third term, i.e., the resonance-type dispersion.

Eq. (4) is of significance in that it clearly distinguishes the Fröhlich model from the Debye and the Lorentz ones. It should also be noted that the second shifted Debye term in Eq. (4) is not passive since it leads to a positive imaginary part of the permittivity as the frequency is below ω_0. Thus, the Fröhlich model can be interpreted as a combination of a shifted passive Debye-type dispersion, a shifted active Debye-type dispersion, and a Lorentz-type dispersion.

2.2 Maxwell Garnett mixing rule

For a two-phase composite with spherical inclusions shown in Fig. 2, several classical mixing rules are available to approximate the effective permittivity ε_{eff}. Maxwell Garnett formula is perhaps the most commonly-applied mixing

rule, which reads [29]

$$\varepsilon_{\text{eff}} = \varepsilon_{\text{e}} + 3p\varepsilon_{\text{e}} \frac{\varepsilon_{\text{i}} - \varepsilon_{\text{e}}}{\varepsilon_{\text{i}} + 2\varepsilon_{\text{e}} - p(\varepsilon_{\text{i}} - \varepsilon_{\text{e}})}. \tag{5}$$

where ε_{e} is the relative permittivity of the host medium; ε_{i} and p denote the relative permittivity and the volume fraction of the inclusions. It is derived by substituting each sphere by an equivalent dipole moment. By further averaging all the dipole moments into the electric polarization, the ε_{eff} can be determined [29, 32, and 33]. Two major assumptions are made during the derivation. One is that the spheres should be small enough with respect to the external electric field so that they can be replaced by a dipole moment. The other is that the spherical inclusions should be well separated from each other so that the interactions among each sphere can be neglected. Therefore, the Maxwell Garnett mixing formula is considered as a good predictor for the non-clustered dilute composites in the quasi-static region.

2.3 Dispersion of the mixture

The composite shown in Fig. 2 whose inclusions display an interesting dispersion is often categorized as raisin pudding mixture, while the complementary structure is termed as Swiss cheese mixture (neutral inclusions and a dispersive host medium). Let us consider here several dielectric raisin mixtures in the quasi-static region. The dispersion of their inclusions is assumed to follow the Debye model, the Lorentz model, and the Fröhlich model, respectively; the background medium is assumed non-dispersive. By the Maxwell Garnett rule, the corresponding effective permittivities are derived in order to discuss the effect of mixing on the dispersion mechanism. It should be noted that the results in subsections 2.3.1 and 2.3.2 were originally presented in [29], and subsection 2.3.3 summarizes the main results in [P1].

2.3.1 The Debye model v.s. the Debye raisin mixture

When the spherical inclusions display the Debye-type dispersion (Eq. (1)), the effective permittivity of the corresponding raisin mixture reads according to the Maxwell Garnett rule [29]

$$\varepsilon_{\text{eff}}(\omega) = \varepsilon_{\infty,\text{eff}} + \frac{\varepsilon_{\text{s,eff}} - \varepsilon_{\infty,\text{eff}}}{1 + j\omega\tau_{\text{eff}}}, \tag{6-1}$$

where the modified parameters read

$$\varepsilon_{\infty,\text{eff}} = \varepsilon_{\text{e}} + 3p\varepsilon_{\text{e}} \frac{\varepsilon_{\infty} - \varepsilon_{\text{e}}}{\varepsilon_{\infty} + 2\varepsilon_{\text{e}} - p(\varepsilon_{\infty} - \varepsilon_{\text{e}})}, \tag{6-2}$$

$$\varepsilon_{\text{s,eff}} = \varepsilon_{\text{e}} + 3p\varepsilon_{\text{e}} \frac{\varepsilon_{\text{s}} - \varepsilon_{\text{e}}}{\varepsilon_{\text{s}} + 2\varepsilon_{\text{e}} - p(\varepsilon_{\text{s}} - \varepsilon_{\text{e}})}, \tag{6-3}$$

$$\tau_{\text{eff}} = \tau \frac{\varepsilon_\infty + 2\varepsilon_\text{e} - p(\varepsilon_\infty - \varepsilon_\text{e})}{\varepsilon_\text{s} + 2\varepsilon_\text{e} - p(\varepsilon_\text{s} - \varepsilon_\text{e})}. \tag{6-4}$$

It is clear that after mixing the dielectric dispersion remains the Debye type as the inclusions, but the characteristic parameters vary. In particular, the relaxation frequency increases after the mixing, since ε_s should be larger than ε_∞ in order that the Debye model is passive.

2.3.2 The Lorentz model v.s. the Lorentz raisin mixture

Similarly to the Debye case, the Lorentz raisin mixture also retains the same dispersion mechanism as its inclusions, and the modified characteristic parameters are specified as follows [29]

$$\varepsilon_{\infty,\text{eff}} = \varepsilon_\text{e} + 3p\varepsilon_\text{e} \frac{\varepsilon_\infty - \varepsilon_\text{e}}{\varepsilon_\infty + 2\varepsilon_\text{e} - p(\varepsilon_\infty - \varepsilon_\text{e})}, \tag{7-1}$$

$$\omega_{\text{p,eff}} = \sqrt{p} \frac{3\varepsilon_\text{e}}{\varepsilon_\infty + 2\varepsilon_\text{e} - p(\varepsilon_\infty - \varepsilon_\text{e})} \omega_\text{p}, \tag{7-2}$$

$$\omega_{\text{o,eff}}^2 = \omega_\text{o}^2 + \frac{1-p}{\varepsilon_\infty + 2\varepsilon_\text{e} - p(\varepsilon_\infty - \varepsilon_\text{e})} \omega_\text{p}^2, \tag{7-3}$$

$$\nu_{\text{eff}} = \nu. \tag{7-4}$$

The mixture exhibits a decreased plasma frequency, resulting from a smaller number density of the electrons in the mixture. The resonance frequency after mixing shows an up-shift, which decreases with increasing volume fraction p. As a special case, the effective permittivity of the Drude raisin mixture follows the Lorentz model, where all the transformed parameters remain as Eq. (7-1)–Eq. (7-4).

2.3.3 The Fröhlich model v.s. the Fröhlich raisin mixture [P1]

Different from the previous cases, the Fröhlich raisin mixture does not display the same dispersion as its inclusions. Based on the Maxwell Garnett mixing rule, the effective permittivity reads

$$\begin{aligned}\varepsilon_{\text{eff}}(\omega) = \varepsilon_{\infty,\text{FR}} + \frac{1}{2}\Delta\varepsilon_{\text{FR}} \left(\frac{1 + j\omega_{\text{o,FR}}\tau_{\text{FR}}}{1 + j(\omega + \omega_{\text{o,FR}})\tau_{\text{FR}}} + \frac{1 - j\omega_{\text{o,FR}}\tau_{\text{FR}}}{1 + j(\omega - \omega_{\text{o,FR}})\tau_{\text{FR}}} \right) - \\ \frac{2j(K^2 - K)\omega_\text{o}^2\tau^3\omega}{(1 + \omega^2\tau^2K^2 + K\omega_\text{o}^2\tau^2 + 2j\omega K\tau)(1 + \omega^2\tau^2K + \omega_\text{o}^2\tau^2 + jK\omega\tau + j\omega\tau)},\end{aligned} \tag{8-1}$$

where $\varepsilon_{\infty,\text{RF}}$ and $\varepsilon_{\text{s,RF}}$ remain as Eq. (6-2) and Eq. (6-3), respectively; other transformed parameters are as follows

$$K = \frac{\varepsilon_\infty(1-p) + \varepsilon_\text{e}(2+p)}{\varepsilon_\text{s}(1-p) + \varepsilon_\text{e}(2+p)}, \tag{8-2}$$

$$\tau_{\text{FR}} = K\tau, \tag{8-3}$$

$$\omega_{0,\mathrm{FR}} = \omega_0 / \sqrt{K}, \tag{8-4}$$

$$\Delta\varepsilon_{\mathrm{FR}} = \varepsilon_{\mathrm{s,FR}} - \varepsilon_{\infty,\mathrm{FR}}. \tag{8-5}$$

It is clearly shown that due to an additional remainder in Eq. (8-1) the dispersion behavior of the Fröhlich raisin mixture does not straightforwardly follow the Fröhlich model.

In order to better characterize the dispersion mechanism of the Fröhlich raisin mixture, Eq. (8-1) is rewritten as

$$\varepsilon_{\mathrm{eff}}(\omega) = \varepsilon_{\infty,\mathrm{FR}} + \frac{A}{\omega - \omega_1} + \frac{B}{\omega - \omega_2}. \tag{9-1}$$

The characteristic parameters ω_1, ω_2, A and B are given, respectively, by

$$\omega_{1,2} = \frac{-j\left[\varepsilon_{\mathrm{e}}(4+2p) + \varepsilon_{\infty}(1-p) + \varepsilon_{\mathrm{s}}(1-p)\right] \pm \sqrt{H}}{2\tau\left[\varepsilon_{\infty}(p-1) - \varepsilon_{\mathrm{e}}(p+2)\right]}, \tag{9-2}$$

$$A, B = 9\varepsilon_{\mathrm{e}}^2 p(\varepsilon_{\infty} - \varepsilon_{\mathrm{s}}) \frac{j\sqrt{H} \pm \left[(1-p)(\varepsilon_{\infty} - \varepsilon_{\mathrm{s}}) + 2\omega_0^2\tau^2(2\varepsilon_{\mathrm{e}} + p\varepsilon_{\mathrm{e}} + \varepsilon_{\infty} - p\varepsilon_{\infty})\right]}{2\tau\left[(2+p)\varepsilon_{\mathrm{e}} + (1-p)\varepsilon_{\infty}\right]^2 \sqrt{H}} \tag{9-3}$$

$$\begin{aligned} H = &-\left[2\varepsilon_{\mathrm{e}}(2+p) + (\varepsilon_{\infty} + \varepsilon_{\mathrm{s}})(1-p)\right]^2 + 4\left[\varepsilon_{\infty}(1-p) + \right. \\ &\left. \varepsilon_{\mathrm{e}}(2+p)\right]\left[\varepsilon_{\mathrm{s}}(1-p) + \varepsilon_{\mathrm{e}}(2+p)\right](1 + \omega_0^2\tau^2). \end{aligned} \tag{9-4}$$

From Eq. (9-2) to Eq. (9-4), it is clear that the properties of the parameters ω_1, ω_2, A and B depend greatly on the sign of H, i.e., Eq. (9-4).

- For dilute mixtures, $H < 0$ and thus the parameters ω_1, ω_2, A and B are simultaneously purely imaginary. Eq. (9-1) thus displays a double-Debye-type dispersion (DDTD). In particular, two Debye-type dispersions, denoted by the second and the third terms of Eq. (9-1), have different signs, and the positive one is smaller in amplitude than the negative one, which ensures that the total dispersion obeys passivity.
- With gradually increasing p, H approaches zero from negative. When H reaches zero, the limiting volume fraction p_{b} can then be analytically derived by letting Eq. (9-4) equal zero, and it reads

$$\begin{aligned} p_{\mathrm{b}} = &\frac{(\varepsilon_{\infty} - \varepsilon_{\mathrm{s}})^2 - 6\omega_0\tau\varepsilon_{\mathrm{e}}\sqrt{(\varepsilon_{\infty} - \varepsilon_{\mathrm{s}})^2(1 + \omega_0^2\tau^2)}}{(\varepsilon_{\infty} - \varepsilon_{\mathrm{s}})^2 - 4\omega_0^2\tau^2(\varepsilon_{\infty} - \varepsilon_{\mathrm{e}})(\varepsilon_{\mathrm{s}} - \varepsilon_{\mathrm{e}})} - \\ &\frac{2\omega_0^2\tau^2\left[(\varepsilon_{\mathrm{s}} + 2\varepsilon_{\mathrm{e}})(\varepsilon_{\infty} - \varepsilon_{\mathrm{e}}) + (\varepsilon_{\infty} + 2\varepsilon_{\mathrm{e}})(\varepsilon_{\mathrm{s}} - \varepsilon_{\mathrm{e}})\right]}{(\varepsilon_{\infty} - \varepsilon_{\mathrm{s}})^2 - 4\omega_0^2\tau^2(\varepsilon_{\infty} - \varepsilon_{\mathrm{e}})(\varepsilon_{\mathrm{s}} - \varepsilon_{\mathrm{e}})}. \end{aligned} \tag{9-5}$$

- When p continues to increase from p_{b}, $H > 0$ so that ω_1, ω_2, A and B are complex, and in particular, $\mathrm{Re}(A) = -\mathrm{Re}(B)$, $\mathrm{Im}(A) = \mathrm{Im}(B)$, $\mathrm{Re}(\omega_1) = -\mathrm{Re}(\omega_2)$ and $\mathrm{Im}(\omega_1) = \mathrm{Im}(\omega_2)$. The mixture then behaves in a more complicated dispersion mechanism — a combination of one Lorentz-type and one shifted passive

Debye-type and one shifted active Debye-type dispersions (LDDD).

- Figs. 5–8 in [P1] clearly visualize the above results.

Finally, it is worth to mention that the DDTD and the LDDD mechanisms are more general, and cannot be reduced to the simple dielectric models except when extra conditions are imposed. For instance, the DDTD is equivalent to the Lorentz dispersion by further forcing the imaginary parts of A and B to be opposite signs; if A and B are real, the LDDD will reduce to the Lorentz model as well.

3. Quasi-dynamic homogenization methods

The effective permittivities by various mixing formulas are often referred as the quasi-static estimate [1, 34–39]. This fact indicates that it is the long-wavelength regime where the mixing formulas are widely adopted. In order to extend their application in a dynamic homogenization, many assumptions have to be made, which in turn limits the practical importance of the mixing formulas in the quasi-dynamic region.

Therefore, several other quasi-dynamic homogenization techniques for the dielectric composites are developed in this chapter. For the composites with finite thickness, four different homogenization models are adopted to describe the macroscopic EM properties of the composites. The effective parameters of the applied homogenization models are then determined based on the transmission and reflection data, i.e., the scattering parameters (S-parameters). Moreover, the presented S-parameter retrieval methods take into account the situation when an obliquely incident plane wave illuminates the composite slabs. Then, for the same structures, a field averaging method is introduced. Finally, the dispersion diagram method is proposed for the infinite simple cubic or square lattice to determine the quasi-dynamic dispersion of the effective permittivity.

3.1 Benchmark problem

3.1.1 Geometry setup [P2–P5]

First of all, a class of geometrically simple dielectric composites, similar to the geometry setup discussed in [P2–P5], is introduced as a benchmark structure in order to illustrate the usage and the problems of the presented homogenization methods.

To reduce the computational duration, the benchmark geometry is constructed in 2D. As shown in Fig. 3, the composite is infinite in one direction (y-direction) and consists of only a few layers in the other direction (x-direction). The unit cell of the composite is composed of a circular disc with relative permittivity ε_i centered in a dielectric square plate (ε_e). The edge length of the unit cell is a, and the circular inclusion occupies the area of the unit cell by a fraction p. One can obtain the same structure by truncating the

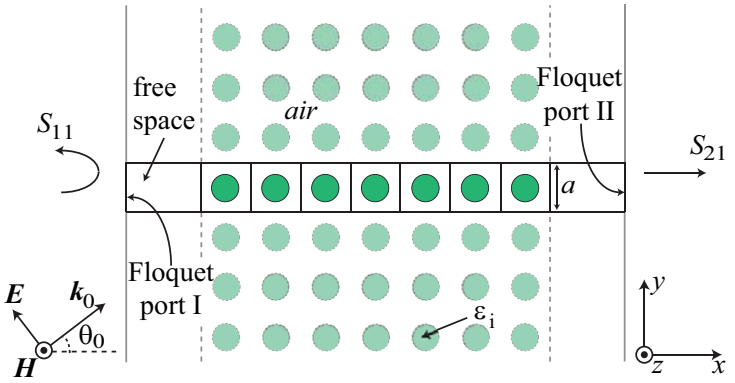

Figure 3 The geometry setup of the considered composite slab. In CST MWS, we only construct one row of consecutive unit cells (the highlighted area).

infinite simple square lattice [40] in the *x*-direction.

Furthermore, an obliquely incident TM_{xy}-polarized plane wave is chosen as the electromagnetic excitation. The TE_{xy}-polarization is not considered since it does not obviously induce strong interactions between electric dipole moments, and the effective permittivity is just the area-averaged result.

In this thesis, the above scenario is constructed in the full wave simulator CST Microwave Studio (MWS) [41]. Only the highlighted area in Fig. 3 needs to be modeled. The composites can then be realized by assigning the unit cell boundary condition to the four bounds in the *y*- and *z*-directions. By applying the Floquet ports and further varying the phase shift between the *y*-directional unit cell boundary pair, a plane wave with incident angle θ_0 is achieved. Moreover, free space of 2 unit cells is added on each side of the slab in the *x*-direction to ensure sufficient attenuation of potential higher order modes. In MWS, both the S-parameters and the field values inside the slab can be simulated and recorded for the retrieval purpose. Parallel studies are performed in another commercial software Comsol Multiphysics 3.5 [42–44, P3].

As a 3D tool, CST MWS cannot model a real 2D structure. However, the *z*-directional thickness d_z in this case only affects the simulation duration but does not introduce extra errors as long as d_z is at least one-mesh-cell long so that the qualities of the tetrahedral mesh cells do not deteriorate. Thus, by reducing the *z*-directional thickness, we can reduce the simulation duration without compromised accuracy.

3.1.2 A reference f_{20} and Lord Rayleigh quasi-static estimate

For convenience, the frequency f is normalized according to a reference f_{20}, which is the frequency when the effective wavelength λ_{eff} inside the slab is 20

times the unit cell edge length a, and we have

$$f_{20} = \frac{c}{20\, a\sqrt{\varepsilon_{\text{eff}}}}, \tag{10}$$

where c is light speed in vacuum, and ε_{eff} denotes the unknown effective permittivity of the composite slab. In order to define f_{20} a reasonable estimate for ε_{eff} is needed.

For an infinite lattice with the same unit cell as in Fig. 3, its (quasi-)static effective permittivity can be estimated by many mixing rules. The 2D Maxwell Garnett mixing formula (ε_{MG}) [29] is perhaps the most commonly-used one. But the 2D Lord Rayleigh formula, which reads [20]

$$\varepsilon_{\text{Ray}} = \varepsilon_{\text{e}} + \frac{2p\varepsilon_{\text{e}}}{\dfrac{\varepsilon_{\text{i}}+\varepsilon_{\text{e}}}{\varepsilon_{\text{i}}-\varepsilon_{\text{e}}} - p - \dfrac{\varepsilon_{\text{i}}-\varepsilon_{\text{e}}}{\varepsilon_{\text{i}}+\varepsilon_{\text{e}}}(0.3058p^4 + 0.0134p^8)}, \tag{11}$$

can actually provide a more accurate estimate ε_{Ray} since it takes into account interactions between the inclusions. Moreover, the difference $\Delta\varepsilon$ (= $\varepsilon_{\text{Ray}} - \varepsilon_{\text{MG}}$) is expected to increase when the inclusion volume fraction p or the inclusion permittivity ε_{i} grows. Fig.4 demonstrates those points.

For the considered finite-thickness slab, Eq. (11) could still supply a good reference to its (quasi-)static ε_{eff}. Moreover, the term 'quasi-dynamic' implies that the homogenization is a dynamic one, but meanwhile is carried out quite close to the quasi-static limit. Thus, in this thesis, the 2D Lord Rayleigh (quasi-)static estimate ε_{Ray} is chosen to approximate the effective permittivity of the composite slab in the quasi-dynamic region. Then, the normalized frequency f/f_{20} can not only show the dispersion of ε_{eff}, but also approximately indicate the ratio between a and λ_{eff}. For instance, a is roughly one-tenth of λ_{eff} when f/f_{20} equals 2.

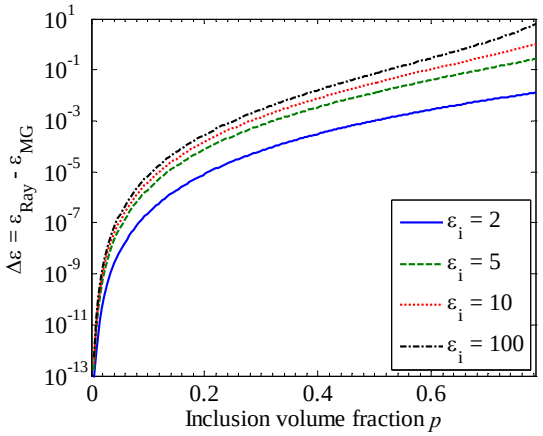

Figure 4 The difference between the Lord Rayleigh (ε_{Ray}) and the Maxwell Garnett (ε_{MG}) estimates, i.e., $\Delta\varepsilon = \varepsilon_{\text{Ray}} - \varepsilon_{\text{Ray}}$, as a function of inclusion volume fraction p for various inclusion permittivity ε_{i}. The permittivity ε_{e} of the background medium is unity.

It is noted that according to our numerous studies, $a/\lambda_{eff} = 1/20$ seems to be a reasonable choice to neglect spatial dispersion when the composite slab behaves like a homogeneous medium. This is the reason we normalize the frequency to f_{20}. Of course, one can choose a looser or stricter normalization, e.g., f_{10} or f_{40}.

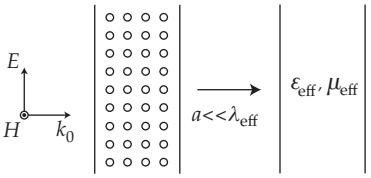

Figure 5 Characterization of the actual composite slab as a homogeneous model with ε_{eff} and μ_{eff} when a plane wave is normally incident on the slab.

3.2 S-parameter retrievals

3.2.1 Homogeneous model and normal incidence (Nicolson–Ross–Weir method)

The classical approach of retrieving the effective parameters ε_{eff} and μ_{eff} from the S-parameters was originally studied by Nicolson, Ross, and Weir [45, 46]. Suppose that a plane wave is normally incident on a composite slab, as shown in Fig. 5. If the inhomogeneity of the slab is much smaller than λ_{eff}, one can treat the real composite with a homogeneous medium with ε_{eff} and μ_{eff}. Thus, the S-parameters from this slab can be formulated as follows

$$S_{11} = \frac{R(1-e^{-j2nk_0d})}{1-R^2e^{-j2nk_0d}}, \tag{12}$$

$$S_{21} = \frac{(1-R^2)e^{-jnk_0d}}{1-R^2e^{-j2nk_0d}}, \tag{13}$$

$$R = \frac{z-1}{z+1}, \tag{14}$$

where n $(=(\varepsilon_{eff}\cdot\mu_{eff})^{1/2})$ and z $(=(\mu_{eff}/\varepsilon_{eff})^{1/2})$ denote refractive index and impedance, R is reflection coefficient across the first boundary between free space and the medium, k_0 is the free-space wave number, and d is the slab thickness.

By inverting Eq. (12) and Eq. (13), one can get the classical NRW method, which reads (where the integer m is the branch index of the logarithmic function)

$$z = \pm\sqrt{\frac{(1+S_{11})^2 - S_{21}^2}{(1-S_{11})^2 - S_{21}^2}}, \tag{15}$$

$$Q = e^{-jnk_0 d} = \frac{S_{21}}{1 - S_{11}(z-1)(z+1)^{-1}}, \tag{16}$$

$$n = \frac{1}{k_0 d}\left\{\left[-\mathrm{Im}\left[\ln(Q)\right] + 2m\pi\right] + j \cdot \mathrm{Re}\left[\ln(Q)\right]\right\}. \tag{17}$$

Branch selection

A closer examination on Eq. (15)–Eq. (17) shows that there are two uncertainties in determining the wave impedance z and the refractive index n. The sign ambiguity in Eq. (15) can be cleared by the requirement $\mathrm{Re}(z) \geq 0$. But how to select the correct branch of the logarithmic function in Eq. (17) is a tougher problem in most applications. For instance, when the NRW method is applied to determine the effective parameters of metamaterials [47–54], the correct branch m of each frequency sample cannot readily be fixed. An iterative method is introduced in [54], which utilizes the mathematical continuity of the exponential function (Eq. (16)) to settle the branch sample by sample, given that the correct branch at the preceding sample is known.

However, since in this chapter the composites are assumed nonmagnetic and non-dissipative, the branch ambiguity only exists for the real part of the refractive index, which can be estimated by the static Lord Rayleigh result, i.e., $n_{EST} = \varepsilon_{Ray}^{1/2}$. For the composite with $\varepsilon_e = 1$, $\varepsilon_i = 10$ and $p = 0.3$, Fig. 6 illustrates the retrieved refractive indices n for different branch m of the logarithmic function in Eq. (17) as well as the estimated n_{EST}. It is clearly shown that at very low frequency, the branch index '$m = 0$' leads to the correct n, and as the frequency grows the expected smooth curve representing the physically reasonable n contains different branch indices m (denoted by various markers and colors). Fortunately, within the selected frequency range, the estimated n_{EST} (black dashed line) is very close to the correct n, and serves as a good baseline to choose the correct branch index m. Thus, the branch uncertainty can be settled by the a priori refractive index $n_{EST} = \varepsilon_{Ray}^{1/2}$.

Fabry–Pérot resonance and the compensation method [P2]

When lossless or low loss dielectric composites with finite thickness are considered, the S-parameter retrieval results will severely be distorted by the Fabry–Pérot resonances (FPRs) [34, 55]. The FPR itself is physical and appears when the slab thickness is an integer multiple of half of the effective wavelength inside the slab. In these situations, the reflections from different boundaries of the slab will cancel each other, resulting in $S_{11} = 0$ and thus the impedance z is singular according to Eq. (15). So the FPR actually comes from the improperly defined impedance z. When a homogeneous material sample is treated by the NRW method, the FPR is also present but its influence on the results is limited in a very narrow frequency band [56]. Unfortunately, if one replaces the sample by a composite of our interest, the results in Fig. 7

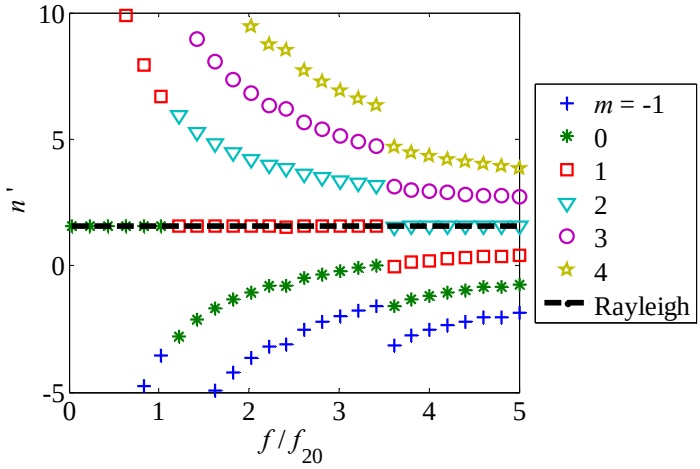

Figure 6 The retrieved refractive index n for different branches m versus the estimated one based on the static Lord Rayleigh formula and nonmagnetic assumption. The black dashed line represents the estimated refractive index, while different markers denote n of the corresponding branch. Within the visualized frequency range, the Rayleigh estimate offers a good baseline to select the correct branch.

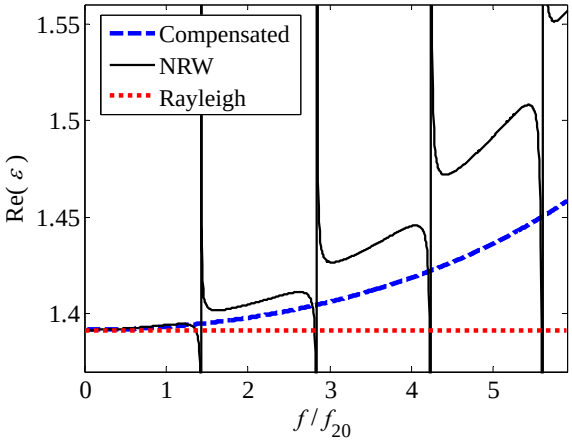

Figure 7 A numerical example of a 7-layer composite slab when p = 0.2, ε_i = 10, and ε_e = 1. Black solid line represents the results by the NRW method; blue dashed line denotes the results by the compensated NRW method, or both-S-parameter method with compensation (BSCM); dotted red line is the Lord Rayleigh estimate.

are distorted by the FPRs over a surprisingly broadband around the resonances, which in turn greatly limits the practical usage of the retrieval results. It is perhaps because the unit cell size is not sufficiently small compared with the effective wavelength, so that many factors, such as the boundary layer effect and spatial dispersion, affect the accuracy of the homogeneous model, and thus influence the quality of the NRW method base on such a model.

On the other hand, the retrieved refractive index seems physically reasonable and free of the FPRs. In order to eliminate the influence of the FPR and

restore physically sound effective medium parameters, a compensation method (or BSCM: both-S-parameter method with compensation) is introduced in this thesis based on the nonmagnetic assumption. Thus we can retrieve the effective permittivity ε_{eff} by the calculated refractive index n, i.e., $\varepsilon_{\text{eff}} = n^2$, and the results are shown in Fig. 7. Moreover, the non-magnetic assumption is quite reasonable for the considered frequency range and the dielectric composites with not very large permittivity contrasts, since the artificial magnetism is the second-order spatial dispersion effect in terms of the ratio between the unit cell dimension and the effective wavelength [2]. Of course, this compensation approach will introduced some errors to the system. But since we are close to the (quasi-)static limit, the error is expected to be negligible [P4].

Retrievals based on parts of the S-parameters [P2]

Based on the nonmagnetic assumption $\mu_{\text{eff}} = 1$, one can retrieve the single unknown ε_{eff} using either S_{11} or S_{21}. At this time, both Eq. (12) and Eq. (13) become functions of only one variable ε_{eff}. One can thus retrieve ε_{eff} by numerically inverting either Eq. (12) or Eq. (13). In order to locate the complex roots of a nonlinear equation with complex coefficients, we numerically separate the equation into real and imaginary parts, and then solve a system of the two nonlinear yet real equations from the separation in a least square sense by the Levenberg–Marquardt algorithm (LMA) [57]. Similar to other minimization algorithms, the LMA finds only a local minimum. Thus, a reasonable initial guess should be provided in order to locate the correct solutions which are physically reasonable. Fortunately, for the considered dielectric composites in the quasi-dynamic region, the dispersive permittivities are expected to increase smoothly and vary in a small dynamic range. Hence, one can choose the static Lord Rayleigh estimate as the initial guess, which will ensure that the LMA can locate the correct solutions. Moreover, it is found that for the normal incidence the retrieval using only S_{21} is more robust than the S_{11} retrieval. Meanwhile, the S_{21} retrieval result agrees well with but is not exactly the same as the permittivity resolved by the BSCM.

In addition, by the definition of the FPR frequency points, i.e., $S_{11} = 0$, an effective wavelength method (EWM) is presented as

$$\varepsilon_{\text{eff}} = \left(\frac{t\lambda_t}{2d} \right)^2, \qquad t = 1, 2, 3... \tag{18}$$

where λ_t is the free space wavelength at the FPR of order t. Although this method is only valid for the retrieval at frequency points corresponding to the FP resonances, it provides a good comparison and validation for the results by other retrieval approaches. The EWM results coincide with those by the S_{11} method and globally display the similar dispersion behaviors as the retrieval results by the S_{21} method and the BSCM.

3.2.2 Homogeneous model and oblique incidence [P5]

Let us go back to Fig. 3 and consider the cases when an obliquely incident plane wave illuminates the composite slab, i.e., $\theta_0 \neq 0$. The effective permittivity of the homogeneous model (H-model) can be derived by the generalized S-parameter retrieval and compensation method, which is given by [P5]

$$z' = \pm\sqrt{\frac{(1+S_{11})^2 - S_{21}^2}{(1-S_{11})^2 - S_{21}^2}}, \tag{19}$$

$$Q = \frac{S_{21}}{1 - S_{11}(z'-1)(z'+1)^{-1}}, \tag{20}$$

$$n' = (k_0 d)^{-1}\left[j\ln(Q) + 2m\pi\right], \tag{21}$$

$$\varepsilon_{\text{eff}}(\theta_0) = \frac{n'^2 + \sin^2\theta_0}{\mu_{\text{eff}}}, \tag{22}$$

where θ_0 is the angle of the incident plane wave, and n' and z' are defined as

$$z' = \frac{z\cos\theta_1}{\cos\theta_0} = \sqrt{\frac{\mu_{\text{eff}}}{\varepsilon_{\text{eff}}}}\frac{\cos\theta_1}{\cos\theta_0}, \qquad n' = n\cos\theta_1 = \sqrt{\varepsilon_{\text{eff}}\mu_{\text{eff}}}\cos\theta_1, \tag{23}$$

where z and n are the ordinary wave impedance and refractive index, and θ_1 represents the effective refractive angle in the slab for the lossless case. For lossy materials, θ_1, still determined by Snell's law [21], is a complex-valued angle without a well-defined physical meaning. Together with the nonmagnetic assumption $\mu_{\text{eff}} = 1$, the dispersion of the effective permittivity at arbitrary incident angle can be calculated. As aforementioned, this approach is also called both-S-parameter method with compensation (BSCM).

Moreover, one can determine $\varepsilon_{\text{eff}}(\omega, \theta_0)$ by the S_{11} method, the S_{21} method, and the EWM generalized into oblique incidence. The retrieval results by different methods are compared in Fig. 8 (same as Figs. 2–3 in [P5]). Finally, several remarks on the retrieval methods are given based on our extensive numerical studies.

- The BSCM can reasonably restore the dielectric dispersion of the considered composites under oblique incidence. All the retrieved permittivities converge to a value slightly larger than the static Rayleigh estimate ε_{Ray} at very low frequency. With the increasing frequency, all the results gradually grow and deviate from one another. This phenomenon due to spatial dispersion is termed as 'angular dispersion' of the effective medium parameters in this thesis.
- The performances of the S_{11} and S_{21} methods clearly depend on the incident angle. The larger the incident angle is, the more (less) robust the S_{11} (S_{21}) method will become.
- The EWM predicts a similar dispersion trend as the BSCM, and its solution quality follows that of the S_{11} method.

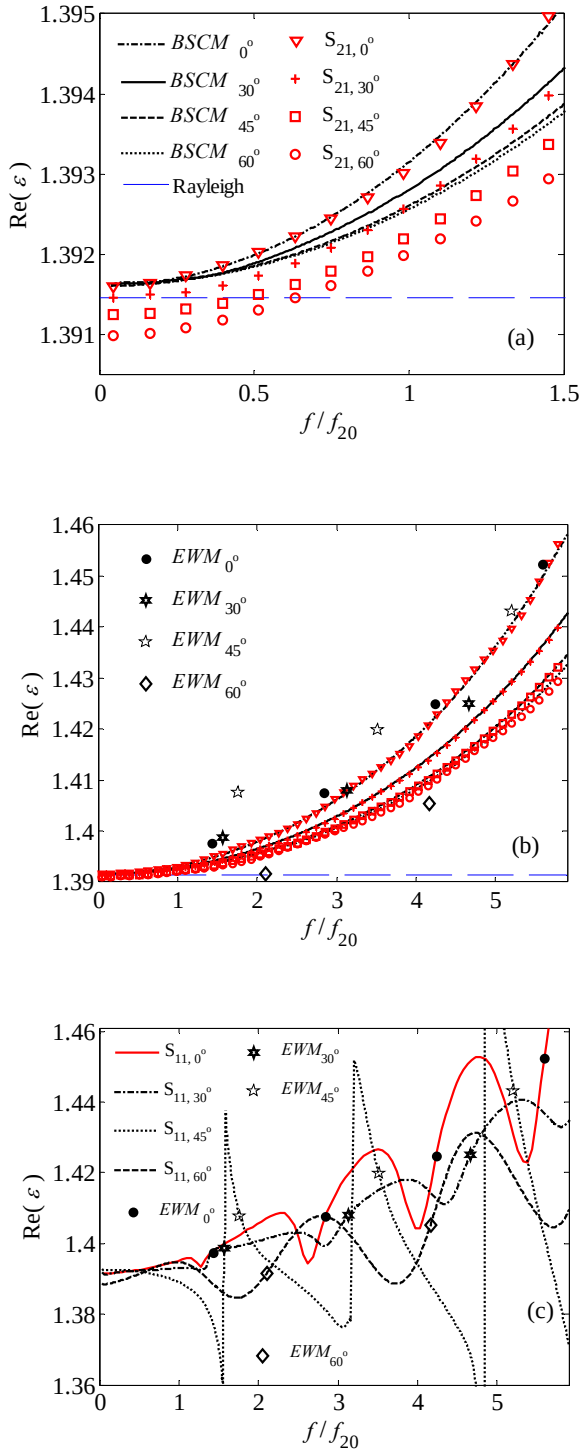

Figure 8 A numerical example of a 7-layer composite slab when p = 0.2, ε_i = 10, and ε_e = 1. (a) Low frequency comparison between the BSCM and the S_{21}-method at θ_0 = 0°, 30°, 45°, and 60°. The blue dashed line indicates the static Lord Rayleigh estimate; (b) and (c) presents the global comparisons among the presented methods [P5].

- Despite similar results, the BSCM and the S_{21} method are intrinsically different, in that the BSCM uses both S-parameters to arrive at Eq. (22) while the S_{21} method only uses S_{21}.
- Angular dispersion reflects the limitations of the homogeneous model and retrieval techniques. When the frequency grows, the dimension of the unit cell becomes no longer sufficiently small compared with the effective wavelength. Spatial dispersion thus becomes non-negligible. In principle, an ideal homogenization cannot be performed in this situation. However, if the homogenization is anyway carried out, unphysical behaviors of the retrieved effective medium parameters are expected, and these unphysical behaviors are also expected to be magnified with increasing frequency. In Fig. 8, the increasingly obvious angular dependence of $\varepsilon_{\mathrm{eff}}$ clearly illustrates this point. This phenomenon also motivates us to apply more complex models to homogenize the composite slab in the following sections to investigate the possibility of suppressing angular dispersion.

3.2.3 Anisotropic model [P3]

Although the unit cell of the composite slab is highly symmetric, the whole structure loses such symmetry due to the finite-thickness in one direction and infinity in the other. When oblique incidence is considered, the isotropic homogeneous model may no longer characterize the finite-thickness slab sufficiently. Instead, an anisotropic model (A-model), with the y-directional permittivity ε_{y} and the x-directional permittivity ε_{x}, is considered. A similar derivation to that in subsection 3.2.2 can be conducted. By redefining n' and z' as (it is noted that despite different definitions, z' and n' are quantitatively equal to those given by Eq. (19) and Eq. (21))

$$z' = \frac{k_1 \cos\theta_1}{\varepsilon_y k_0 \cos\theta_0}, \qquad n' = \frac{k_1 \cos\theta_1}{k_0}, \tag{24}$$

where k_1 is wave number in the anisotropic medium, and follows the corresponding dispersion equation, which reads

$$\frac{k_1^2 \cos^2\theta_1}{\varepsilon_{\mathrm{y}}} + \frac{k_1^2 \sin^2\theta_1}{\varepsilon_{\mathrm{x}}} = \frac{\omega^2}{c^2}. \tag{25}$$

A little algebra based on Eq. (24) and Eq. (25) shows that

$$n' = \sqrt{\frac{\varepsilon_{\mathrm{x}}\varepsilon_{\mathrm{y}}}{\varepsilon_{\mathrm{x}}\cos^2\theta_1 + \varepsilon_{\mathrm{y}}\sin^2\theta_1}}\cos\theta_1\ , \qquad z' = \sqrt{\frac{\varepsilon_{\mathrm{x}}\varepsilon_{\mathrm{y}}}{\varepsilon_{\mathrm{x}}\cos^2\theta_1 + \varepsilon_{\mathrm{y}}\sin^2\theta_1}}\frac{\cos\theta_1}{\varepsilon_{\mathrm{y}}\cos\theta_0}. \tag{26}$$

In addition, the phase matching condition gives

$$\sin^2\theta_1 = \frac{\varepsilon_{\mathrm{x}}\sin^2\theta_0}{\varepsilon_{\mathrm{x}}\varepsilon_{\mathrm{y}} - \left(\varepsilon_{\mathrm{y}} - \varepsilon_{\mathrm{x}}\right)\sin^2\theta_0}. \tag{27}$$

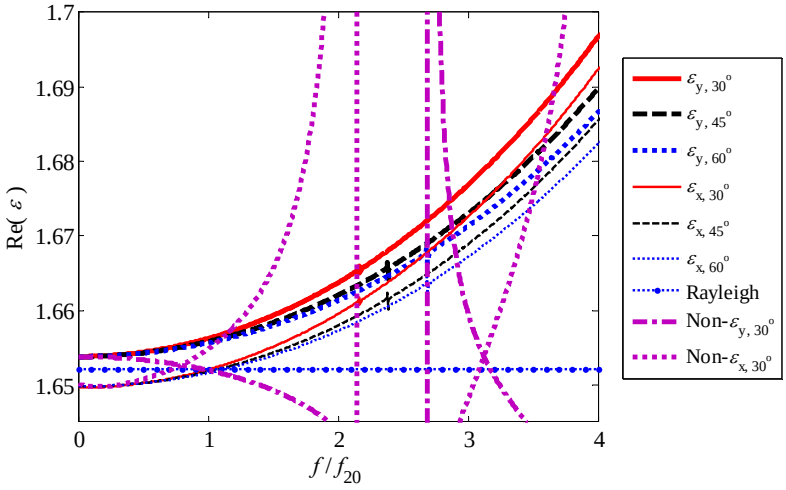

Figure 9 A numerical example of a 5-layer composite slab when p = 0.3, ε_i = 10, and ε_e = 1. The subscripts x and y indicates the x- and y-directional components, and the numerals denote the incident angles. Two purple lines represent the permittivities without compensation at 30°.

Finally, we have [P3]

$$\varepsilon_y = n'/(z'\cos\theta_o), \qquad \varepsilon_x = \sin^2\theta_o/(1-n'z'\cos\theta_o) = \varepsilon_y \sin^2\theta_o/(\varepsilon_y - n'^2). \quad (28)$$

In this case, z' still suffers from the FPR, and it is impossible to cancel z' from the retrieval formulas. But ε_y in Eq. (28) is identical to the non-compensated permittivity ε_{eff} of a homogeneous model in Eq. (23). Therefore, in order to eliminate the distortion from the FPR, ε_y are assumed to equal the compensated ε_{eff} by Eq. (22), and ε_x will consequently get rid of the distortion from the FPR.

The retrieval results are visualized in Fig. 9. It is shown that this compensation method not only eliminates the influence of the FPR, but also yields physically reasonable results. It is also noted that at low frequencies non-$\varepsilon_{y,30°}$ (without compensation) and $\varepsilon_{y,30°}$ (after compensation) converge to the same value slightly larger than the Rayleigh prediction, and so do non-$\varepsilon_{x,30°}$ and $\varepsilon_{x,30°}$ but to a smaller one. This small but noticeable difference between ε_x and ε_y results from the finite thickness of the slab in the x-direction, which breaks the symmetry of the whole structure. Finally, the similar compensations are performed at different θ_o. All the compensated ε_y coincide with each other at low frequency and so do the compensated ε_x. As the frequency grows, angular dispersion is inevitable, and finally prevails over the anisotropy. For instance, at f/f_{20} = 4, the anisotropy measured by $|\varepsilon_{y,30°}-\varepsilon_{x,30°}|$ is smaller than the angular dispersion measured by $|\varepsilon_{y,30°}-\varepsilon_{y,45°}|$.

3.2.4 Stratified model with isotropic or anisotropic boundary layers

According to our recent computational study [43, 58] and previous theoretical literature [59, 60], the permittivity of the outermost boundary layer (with only one neighbor in the x-direction) may show different properties from those of the inner layers (with neighbors on both sides). This motivates us to consider two stratified models with isotropic boundary layers (IBL-model) or anisotropic boundary layers (ABL-model), as shown in Fig. 10.

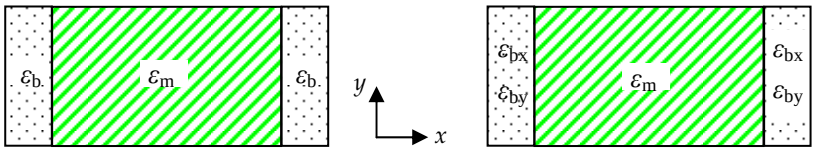

(a) (b)

Figure 10 Two complex models applied to characterize the dielectric slab of our interest. (a) Stratified model with isotropic boundary layers (IBL-model), where ε_b and ε_m are the permittivities of the outermost boundary and inner layers; (b) stratified model with anisotropic boundary layers (ABL-model), where ε_{bx} and ε_{by} are the x- and y-components of the permittivities of the outermost boundary layers, while ε_m is the inner layer permittivity.

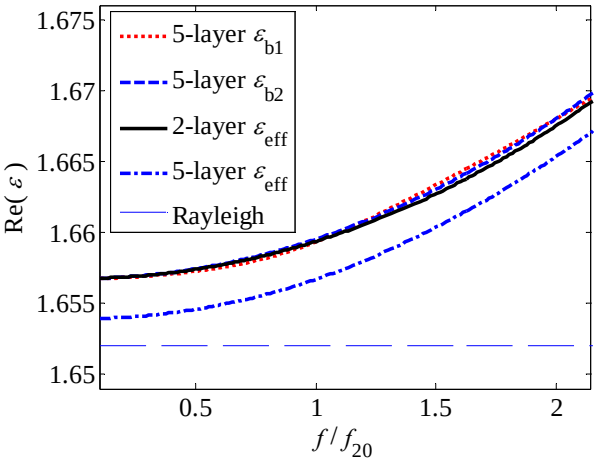

Figure 11 The front and the rear outermost boundary layer permittivities ε_{b1} and ε_{b2} of a 5-layer slab versus ε_{eff} of the H-model for the 2-layer and the 5-layer slabs. The field averaging method [43, P3] is applied to compute these curves.

Several observations have been made in our recent study based on the field averaging method [43, P3] to homogenize the dielectric slab of interest with the IBL-model. Firstly, the permittivities of the outermost boundary layers ε_{b1} and ε_{b2} are roughly identical. Secondly, all the inner layers have the same

permittivity ε_m. Thirdly, ε_{b1} and ε_{b2} are larger than ε_m. Finally, for two slabs with different number of layers, the permittivities of their outermost boundary layers are approximately the same. Fig. 11 confirms that ε_{b1} and ε_{b2} of a 5-layer slab have good agreement with the effective bulk permittivity ε_{eff} for a 2-layer slab, where both layers behave like a boundary layer with only one neighbor in the x-direction. Quantitatively small differences exist among ε_{b1}, ε_{b2} and 2-layer ε_{eff}, but compared with their deviations from the 5-layer ε_{eff}, these differences can be neglected. We can thus resolve ε_b of the IBL-model in Fig. 10(a) by calculating ε_{eff} of the H-model for a 2-layer slab with Eq. (22), namely the 2-layer method; similarly, ε_{bx} and ε_{by} of the ABL-model in Fig. 10(b) can be determined by ε_x and ε_y of the A-model for a 2-layer slab with Eq. (28).

Once ε_b is known, the inner layer permittivity ε_m can be numerically solved by inverting the formulation of the forward propagation matrix method (FPMM) [61]. For a stratified slab with t layers, there are t+1 boundaries which separate the space into t+2 regions. Assuming that each region is anisotropic with $\varepsilon_{i,x}$ and $\varepsilon_{i,y}$ (i = 0, 1, ..., t+1), the FPMM then gives the following equation, which reads

$$\begin{bmatrix} S_{21}\exp(jk_0 d\cos\theta_0) \\ 0 \end{bmatrix} = D_{(t+1)t} D_{t(t-1)} \cdots D_{(i+1)i} \cdots D_{10} \begin{bmatrix} 1 \\ S_{11} \end{bmatrix}, \tag{29}$$

where k_0 and θ_0 are the wave number and the incident angle of the incoming plane wave in region 0 (free space), and d is the total thickness of the stratified slab in the x-direction. Also, the forward propagation matrix $D_{(i+1)i}$ reads

$$D_{(i+1)i} = w \cdot \begin{bmatrix} \exp[jd_i(k_{i+1}\cos\theta_{i+1} - k_i\cos\theta_i)] & R_{(i+1)i}\exp[jd_i(k_{i+1}\cos\theta_{i+1} + k_i\cos\theta_i)] \\ R_{(i+1)i}\exp[-jd_i(k_{i+1}\cos\theta_{i+1} + k_i\cos\theta_i)] & \exp[-jd_i(k_{i+1}\cos\theta_{i+1} - k_i\cos\theta_i)] \end{bmatrix}, \tag{30}$$

$$w = \frac{1 + p_{(i+1)i}}{2}, \quad R_{(i+1)i} = \frac{p_{(i+1)i} - 1}{p_{(i+1)i} + 1}, \quad p_{(i+1)i} = \frac{k_i \cos\theta_i \cdot \varepsilon_{i+1,y}}{k_{i+1}\cos\theta_{i+1} \cdot \varepsilon_{i,y}}, \tag{31}$$

$$k_i = k_0 \sqrt{\frac{\varepsilon_{i,x}\varepsilon_{i,y}}{\varepsilon_{i,x}\cos^2\theta_i + \varepsilon_{i,y}\sin^2\theta_i}}, \tag{32}$$

$$\sin^2\theta_i = \frac{\varepsilon_{i,x}\sin^2\theta_0}{\varepsilon_{i,x}\varepsilon_{i,y} - (\varepsilon_{i,y} - \varepsilon_{i,x})\sin^2\theta_0}, \tag{33}$$

where k_i and θ_i defined in Eq. (32) and Eq. (33) are the wave number and the propagation angle (in lossless cases) of the wave in region i, $R_{(i+1)i}$, caused by the boundary separating the regions i and i+1, represents the reflection coefficient for the wave in region i, and d_i denotes the location of the i^{th} boundary in the x-direction. In particular, we assume that d_0 = 0.

For the 3-layer slab shown in Fig. 10 whose boundary layer permittivity has

already been determined, Eq. (29) then reduces to a system of two equations with only one unknown, i.e., the inner layer permittivity ε_m, which reads

$$f_1(\varepsilon_m) = S_{11}, \quad f_2(\varepsilon_m) = S_{21}. \tag{34}$$

One can then numerically determine the frequency dependence of ε_m by letting the following function reach its minimum at different frequencies,

$$\left|\mathrm{Re}\left(f_1(\varepsilon_m) - S_{11}\right)\right| + \left|\mathrm{Im}\left(f_1(\varepsilon_m) - S_{11}\right)\right| + \left|\mathrm{Re}\left(f_2(\varepsilon_m) - S_{21}\right)\right| + \left|\mathrm{Im}\left(f_2(\varepsilon_m) - S_{21}\right)\right|. \tag{35}$$

In order to locate the correct minimum of Eq. (35), one needs to identify a reasonable search interval. Based on the second formula of Eq. (34), one can use the LMA to numerically solve the unknown inner layer permittivity, denoted as ε_m'. As shown in Fig. 8(b), the result by the S_{21} method is globally consistent with the physically reasonable one determined by the BSCM. Analogically, the numerically determined ε_m' from S_{21} in this case provides a priori knowledge for the physically reasonable result. One can then construct the search interval as $[\varepsilon_m'-\delta, \varepsilon_m'+\delta]$, where δ is a positive real constant. Within the constructed interval with a properly-chosen δ, one can locally minimize Eq. (35) to determine the frequency dependence of ε_m.

In the presence of noise, the retrieval method presented for the stratified models is expected to be less stable than those for the homogeneous and the anisotropic models, since it may suffer from numerical instabilities. For instance, the search interval of the minimization algorithm may contain multiple minima due to noise in the measured S-parameters. Moreover, one may speculate that for the IBL-model ε_b and ε_m can be solved by the direct numerical inversion of Eq. (29), which in this case is a system of two equations with two unknowns. However, the non-unique solutions of Eq. (29) make the direct numerical inversion unreliable.

As a numerical example, the determined model parameters for the IBL- and ABL-models, when a 5-layer composite slab with p = 0.3, ε_i = 10, and ε_e = 1 is considered, are visualized in Fig. 12 and Fig. 13, respectively.

For the IBL-model, it can be seen that different from ε_b, the retrieved ε_m for different θ_0 do not converge to the same value at the low frequencies, which is not due to the imprecision of the 2-layer method since any potential homogenization inaccuracies including the retrieval method and spatial dispersion can be neglected in the static or quasi-static region. Hence, this low-frequency divergence in Fig. 12 indicates that the stratified model with isotropic boundary layers has inherent deficiencies in describing the dielectric-composite slabs under oblique incidence.

The comparison between retrieved ε_m for different θ_0 in Fig. 12 and Fig. 13 indicates that if a stratified model is applied to the dielectric-composite slab under oblique incidence, the separated boundary layers should be anisotropic in order to ensure the retrieved model parameters to be physically reasonable. In addition, the ABL-model is found to be able to slightly suppress the

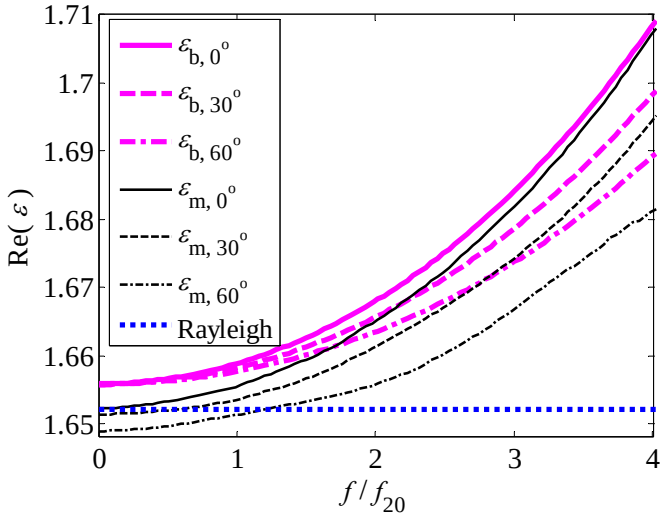

Figure 12 The retrieved permittivities of the inner and the boundary layers at various incident angles. The Lord Rayleigh estimate is shown as the dot markers; and the subscripts b, m, and numeral stand for the boundary layer, the inner layer, and the incident angle, respectively.

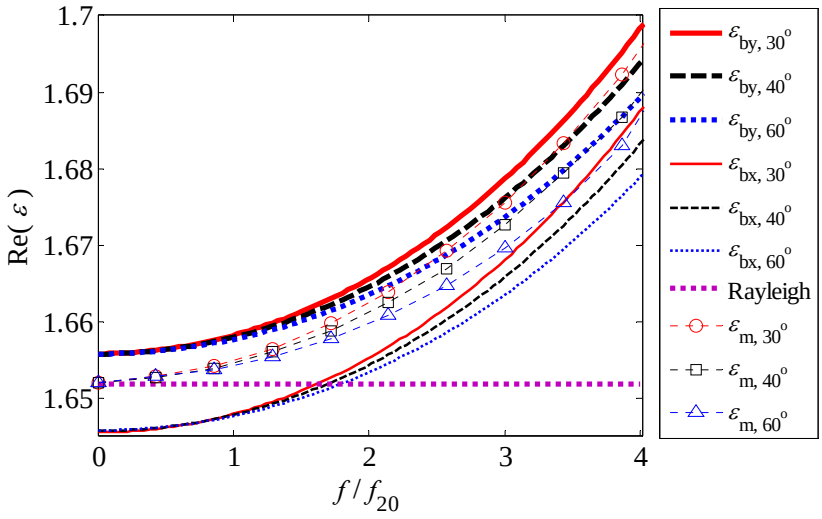

Figure 13 Retrieved angle-dependent ε_{bx}, ε_{by} and ε_{m} for different incident angles θ_o. The subscript b, m, x, y, and numerals denote the boundary layer, the inner layer, *x*-direction, *y*-direction and the incident angle, respectively.

angular dispersion. For instance, as shown in Fig. 9 and Fig. 13, $|\varepsilon_{y,\,30^\circ} - \varepsilon_{y,\,60^\circ}| = 0.0104$ for the A-model when $f/f_{20} = 4$, whereas $|\varepsilon_{by,\,30^\circ} - \varepsilon_{by,\,60^\circ}| = 0.0088$ for the ABL-model.

Let us conclude this section by some remarks. All the derived S-parameter retrievals are either the analytical or numerical inversion of the formulism of a forward propagation problem. The additionally introduced methods (the compensation method and the 2-layer method) aiming at restoring reasonable dispersions of the effective permittivities will inevitably bring into the system some errors, which somehow reflect or measure the imperfection of the quasi-dynamic homogenization theory, including the applied retrieval methods and homogenization models. Obviously, all the proposed methods will lose their physical sense in the full dynamic region. But in the quasi-dynamic region which is close to the quasi-static limit, the homogenization results still have the predictive power despite the gradually deteriorating accuracy. Moreover, a criterion is introduced in Chapter 4 to measure this reduced accuracy of the applied homogenization as the frequency increases.

Finally, to define a boundary for a heterogeneous medium is not as obvious as for a homogeneous material. For our composite slab, this fact would give additional freedom in defining its thickness d. It would be an interesting future work to investigate the possibility to reduce or even eliminate the FPR effects by varying the slab thickness. It should be noted that the compensation method is proposed not only to eliminate the FPR effects, but also to recover the retrieved unphysical effective permeability, which decreases from unity as the frequency grows.

3.3 Field averaging method [P3]

While the S-parameter retrieval method tries to homogenize the composite from outside, another strategy would be to perform the characterization from inside. The field averaging [62–68] is such a method. In this thesis, a straightforward procedure is applied based on the constitutive relation between the local electric displacement and the local electric fields at a point $\boldsymbol{r}$: $\mathbf{D}(\boldsymbol{r}) = \varepsilon(\boldsymbol{r})\mathbf{E}(\boldsymbol{r})$. Then, the effective permittivity can be defined as the ratio between the (area-/volume-)averaged electric displacement and electric fields:

$$\langle \mathbf{D} \rangle = \varepsilon_{\text{eff}} \varepsilon_0 \langle \mathbf{E} \rangle \quad \Leftrightarrow \quad \varepsilon_{\text{eff}} = \frac{\iint_S D_i dS}{\varepsilon_0 \iint_S E_i dS}, \tag{36}$$

where the subscript i denotes different components of the electric and the displacement fields, and the surface integrations are carried out in an area S. The electric and the corresponding displacement fields, when the composite

slab is illuminated by a plane wave with an arbitrary incident angle, can be simulated and recorded by e.g., the full wave simulator Comsol Multiphysics 3.5 [42].

The advantage of this method is that one can freely choose the area (or volume in 3D) of interest and polarization direction to carry out the integration. Let us take the composite shown in Fig. 3 as an example, and concentrate on the case when the slab is illuminated by a normally incident plane wave. If a homogeneous medium is applied to model the real composite slab, one can select the total area of the slab as the integration area S. We can then study the effect of layer number on the homogenization results. It is shown in [P3] that at lower frequencies the effective permittivity is larger than the static Lord Rayleigh estimate, and will gradually converge to this estimate when the slab consists of more and more layers. This point, illustrated by Fig. 8 in [P3], implies that a sufficient amount of layers is required for the slab to behave as a bulk material.

Alternatively, one can carry out the integration over each layer of the slab in order to investigate the electrical properties of individual layer. It turns out that the outermost boundary layers exhibit larger electrical responses than all the other inner layers, whose effective permittivities are roughly identical and converge to the static Lord Rayleigh estimate at lower frequencies. This point suggests that the IBM-model in Fig. 10(a) could be another reasonable homogenization model for the composite slab illuminated by a normally incident plane wave. It also explains the difference between the effective permittivity and the static Lord Rayleigh estimate at lower frequencies when the homogeneous model is applied. Fig. 9 in [P3] clearly illustrates these points.

Moreover, the anisotropy of the slab or individual layer can be studied when an obliquely incident plane wave is considered. In this case, we can integrate different components of the electric and the corresponding displacement fields over the area S of interest. For instance, one can analyze the anisotropy of the outermost boundary layer, i.e., ε_{bx} and ε_{by} in Fig. 10(b), by letting the subscript i in Eq. (36) be x and y, respectively.

In general, the field averaging method is of significance since it not only gives us motivation and evidence to apply more complicated homogenization models, i.e., the A-, the IBL-, and the ABL-models, but also provides a good comparison for the retrieval results based on the S-parameters. Fig. 11 in [P3] illustrates such a comparison between two homogenization methods for a class of 3D dielectric composites illuminated by a normally incident plane wave. The results are consistent with those discussed in the following subsection 4.2 of this thesis.

3.4 Dispersion diagram method [P2]

When an infinite simple square (or cubic in 3D) lattice with the same unit cell as shown in Fig. 3 is considered, it is impossible to determine the effective permittivity based on the S-parameters. Meanwhile, it is not easy to numerically implement the field averaging method since a proper electromagnetic excitation is not readily available.

Suppose that the effective refractive index n of such a structure can be defined, the frequency dependence of n can be addressed as long as the ka–βa dispersion diagram is obtained, given that the effective wave number β is related to the free space wave number k by $\beta = kn$. Here, a is the edge length of the unit cell. By the nonmagnetic assumption $\mu_{\text{eff}} = 1$, one can then determine the effective permittivity, i.e., $\varepsilon_{\text{eff}} = (\beta/k)^2$.

For an infinite lattice composed of nonmagnetic materials, the following eigenfunction equation can be derived from Maxwell equations [5], and it reads

$$\nabla \times \left[\frac{1}{\varepsilon(\boldsymbol{r})} \nabla \times \mathbf{H}(\boldsymbol{r}) \right] = \frac{\omega^2}{c^2} \mathbf{H}(\boldsymbol{r}), \tag{37}$$

where $\mathbf{H}(\boldsymbol{r})$ denotes the spatial field pattern of the harmonic mode, c is the free space light speed, ω represents the eigenfrequency and $\boldsymbol{r}$ denotes a point inside the unit cell. Only the TEM mode $\mathbf{H}(\boldsymbol{r}) = \mathbf{H}_0 e^{-j\beta a}$ needs to be considered here. Then according to Eq. (37), under a certain propagation direction, the eigenfrequencies ω (or $k{\cdot}c$) can be solved by giving different phase shifts βa. The desired ka–βa dispersion diagram can thus be generated.

In practice, one can conveniently generate the desired dispersion diagram for the aforementioned infinite simple square lattice using the commercial full wave simulators. In CST MWS, for example, the lattice can be realized by assigning the periodic boundary condition to its unit cell's boundaries in the $\pm x$- and $\pm y$-directions. A certain propagation direction can thus be specified by systematically varying two phase shifts $\beta_x a$ and $\beta_y a$ between the periodic boundary pairs in the x- and y-directions. Then one can use the CST Eigenmode solver to calculate the corresponding eigenfrequencies for different modes. Moreover, the computed field pattern is utilized to identify the direction of the retrieved ε_{eff}. Although this method targets the infinite simple square (or cubic) lattice, it still offers a good reference for the dispersion of the effective permittivity of the composite slab of our interest. The comparison between the dispersion diagram method and the S-parameter retrieval is illustrated by Figs. 7–10 in [P2].

4. Explorations based on homogenization results

In this chapter, we apply the homogenization techniques developed in the previous chapters to explore several important issues related to the quasi-dynamic homogenization. Firstly, the so-called quasi-static limit for the benchmark geometry is quantitatively investigated by defining a certain satisfactory accuracy [P2, P5]. Secondly, the performance of different homogenization models under oblique incidence is evaluated based on a model evaluation process (MEP) [58].

On the other hand, the dynamic evolution of electromagnetic waves in a dispersive dielectric composite is of practical importance since it could model many realistic propagation problems. Suppose that the space is filled with a certain dielectric composite that can effectively be described as a homogeneous isotropic medium. Then the temporal evolution of an electromagnetic pulse in this composite can be calculated with the aid of Fast Fourier Transform (FFT), once the dispersion of the effective permittivity of the composite is determined [P6, P7].

4.1 Upper frequency limit of the Quasi-static estimate [P2, P5]

As shown in Fig. 8, when the frequency grows, the dispersive $\varepsilon_{\mathrm{eff}}$ grows monotonically and deviates from the (quasi-)static Lord Rayleigh estimate, which implies that the accuracy of the quasi-static estimate describing the electric response of the composite slab in Fig. 3 becomes worse. It is, therefore, important to find the dynamic trust region of the quasi-static estimate for the considered slabs. In other words, we need to locate the upper frequency limit of this dynamic trust region. Hence, a proper criterion or satisfactory accuracy has to be defined in order to quantitatively determine such a limiting frequency. Moreover, it is important to identify the dependence of the limiting frequency on the properties of the composite slab, i.e., the permittivity ε_{i} and the filling fraction p of the inclusions.

To quantify this problem, we specify the procedure as follows:

- Define the limiting frequency f_{L}, at which $(\varepsilon_{\mathrm{eff}}-\varepsilon_{\mathrm{Ray}})/\varepsilon_{\mathrm{Ray}}$ is equal to a predefined satisfactory tolerance;
- Collect sufficient simulated S-parameters form the composite slabs with varying ε_{i} and p;

- Retrieve the dispersive effective permittivities by the BSCM for each combination of ε_i and p;
- Design an interpolation function F_1 of frequency for the retrieved effective permittivity, and fit the coefficients of F_1 for each combination of ε_i and p. Note: the coefficients of F_1 are functions of ε_i and p;
- Design interpolation functions F_2 and F_3 for the coefficients of F_1, and fit the corresponding coefficients of F_2 and F_3, respectively. Thus, the fitted F_1, whose coefficients are expressed as the fitted F_2 and F_3, can reveal the dependence of f_L on ε_i and p.

Following the above procedure, we first define the relative difference between ε_{Ray} and the retrieved ε_{eff} as $(\varepsilon_{eff}-\varepsilon_{Ray})/\varepsilon_{Ray}$, and choose a 1% relative difference as the satisfactory tolerance. We further define the limiting frequency meeting this criterion as f_L, and thus the normalized upper frequency limit is denoted as f_L/f_{20}. Below this limit, the largest relative deviation $\Delta\varepsilon/\varepsilon_{Ray}$ among the retrieved ε_{eff} at various θ_0 is also less than the 1% tolerance, as shown in Fig. 8. Spatial dispersion can thus be neglected. We will hereafter express f_L/f_{20} as a function of the inclusion area fraction p and relative permittivity ε_i.

To build the desired function, we need to repeat the full wave simulation and the retrieval by the BSCM for different p and ε_i to collect sufficient data for the fitting purpose. In particular, we choose ε_i = 10, 20, 30, and 60, and for each ε_i, 9 samples from 0.1 to 0.5 are assigned to p. Only the normal incidence needs to be considered since it leads to the largest deviation from ε_{Ray}. Thus, we have 36 sets of data points for the dispersive $\varepsilon_{eff}(f/f_{20})$.

Then, we construct the interpolation function for ε_{eff} by adding a higher-order correction term to the static one, and it reads

$$\varepsilon_{eff}\left(f/f_{20}\right)=\alpha_0+\alpha_2\cdot\left(f/f_{20}\right)^2, \tag{38}$$

where α_0 represents the static term (and can be assumed to follow the Lord Rayleigh formula), while the quadratic term denotes the electric quadrupole and the magnetic dipole corrections [69]. Since we are close to the quasi-static limit, higher-order multipole interactions can be neglected. The coefficients α_0 and α_2 are then determined using the MATLAB curve fitting tool [70]. We thus have 36 data points for each coefficient in Eq. (38).

Next, we proceed to build interpolation functions of p and ε_i for the coefficients α_0 and α_2, respectively. For α_0, we use a function α_0' based on the Lord Rayleigh formula, which reads

$$\alpha_0' = b_1+\frac{p}{b_2(\varepsilon_i+1)(\varepsilon_i-1)^{-1}-b_3p-(\varepsilon_i-1)(\varepsilon_i+1)^{-1}(b_4p^4+b_5p^8)}. \tag{39}$$

For α_2, we choose a polynomial function (α_2') of p and ε_i, because better fit-

ting functions, whose constituent terms have obvious physical interpretations, are not readily available, and it reads

$$\alpha_2' = q_{00} + q_{10}p + q_{01}\varepsilon_i + q_{20}p^2 + q_{11}p\varepsilon_i + q_{02}\varepsilon_i^2 + q_{30}p^3 + q_{21}p^2\varepsilon_i + q_{12}p\varepsilon_i^2. \quad (40)$$

The MATLAB surface fitting tool is then applied to optimize the coefficients of these fitting functions (Eq. (39) and Eq. (40)) in a least square sense.

We then accomplish the interpolation function to approximate the dispersive ε_{eff} of the composite slab with $0.1 < p < 0.5$ and $10 < \varepsilon_i < 60$, which reads

$$\varepsilon_{eff}\left(f/f_{20},\, p,\, \varepsilon_i\right) = \alpha_0' + \alpha_2' \cdot \left(f/f_{20}\right)^2, \quad (41)$$

where α_0' and α_2' are functions of p and ε_i. Let us now consider the limit f_L/f_{20}. Together with the defined 1% tolerance and Eq. (41), we have

$$\frac{f_L}{f_{20}} = \sqrt{\frac{1.01\varepsilon_{Ray} - \alpha_0'}{\alpha_2'}}. \quad (42)$$

Finally, Eq. (42) is the established interpolation function to analyze the f_L/f_{20} for the considered composite slabs with the applicable range of $0.1 < p < 0.5$ and $10 < \varepsilon_i < 60$. The relevant results can be found in [P5].

4.2 Homogenization model evaluation

If a homogenization model is applied to describe the electromagnetic (EM) properties of the composite, the quality of the model should not vary with the observation angles of the EM fields. Thus, it is crucial to examine its validity by evaluating the performance of the model at different incident angles of an incoming plane wave.

To this purpose, there are two schemes. One is to first analytically calculate the S-parameters at different incident angles θ_0 for the model with the parameters resolved at normal incidence. By comparing at various θ_0 the differences between the above calculated S-parameters and those from the full wave simulation, the angle dependence of the model performance can be studied. The other one is to check whether the retrieved model parameters depend on the incident angle θ_0. It requires the retrieval methods taking into account the off-normal incident cases.

In Chapter 3, four homogenization models were applied to describe the effective permittivity of the composite slab of our interest. The dependence of the parameters of these models on the incident angle will be investigated in this subsection.

For two isotropic models, i.e., H- and IBL-models, the unknown model parameters are first retrieved at the normal incidence. The S-parameters at different θ_0 are then calculated by the FPMM for these two derived models, and compared with corresponding simulated results from CST MWS. If the dif-

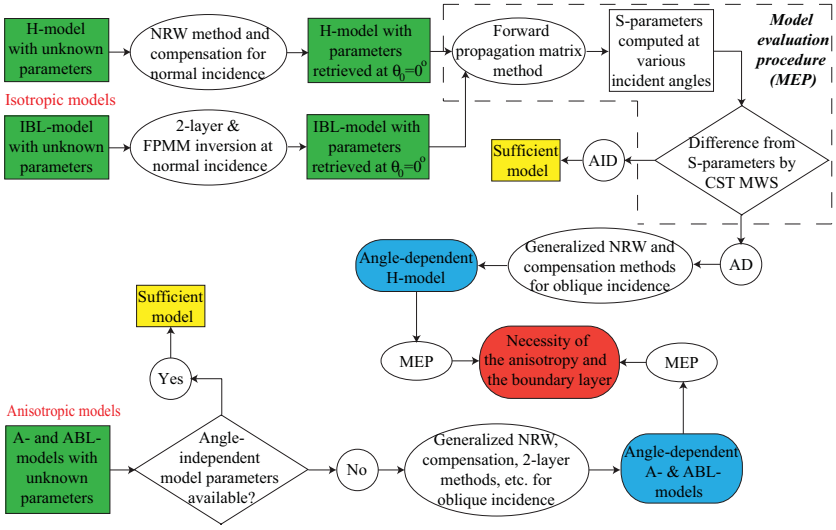

Figure 14 Flow chart as the skeleton of this subsection where AD and AID are short for angle dependent and angle independent. The process in dashed box is the model evaluation process (MEP), which includes the S-parameters computation for a derived model and the comparison with the S-parameters by the full wave simulator (CST MWS). Since the retrieved angle-dependent parameters of the IBL-model display an unphysical low-frequency divergence, it is absent from the final comparison highlighted by the red box. The model abbreviations are explained in Chapter 3.

ference between the calculated S-parameters by FPMM and those from simulation is roughly independent of the incident angle, the model turns out to be sufficient to describe the composite slab. Otherwise, angle-dependent model parameters will be computed based on the S-parameters (see section 3.2).

On the other hand, several attempts are made to find angle-independent parameters for two anisotropic models, i.e., the A- and ABL-models. If such efforts fail, the angle-dependent parameters of these models will be calculated based on the S-parameters (see section 3.2). Fig. 14 visualizes the whole model evaluation procedure as a flow chart. In addition, we define a model evaluation process (MEP), which includes three steps: first, the S-parameters for the model with derived parameters are calculated using the FPMM; second, the difference between the above calculated S-parameters with those by the full wave simulator is computed; third, the dependence of the computed difference on the incident angle is evaluated. In this subsection, a 5-layer composite slab with p = 0.3, ε_i = 10, and ε_e = 1 is considered.

4.2.1 H-model and IBL-model

The permittivity of the H-model under normal incidence $\varepsilon_{eff}(\theta_0 = 0^o)$ is first retrieved by Eq. (22). Suppose that the model parameters are independent of

θ_o, the S-parameters from this H-model with $\varepsilon_{eff}(\theta_o = 0°)$ can respectively be calculated using the FPMM when the incident TM_{xy}-polarized plane wave illuminates the slab with $\theta_o = 0°$, 30°, and 60°, and thus compared with the simulated S-parameters. For convenience, we define the S-parameter difference as the sum of the amplitudes of the S_{11} difference and the S_{21} difference, i.e., $|\Delta S_{11}|+|\Delta S_{21}|$. Such differences, when θ_o respectively equals 0°, 30°, and 60°, are visualized with the red dashed lines in Fig. 15.

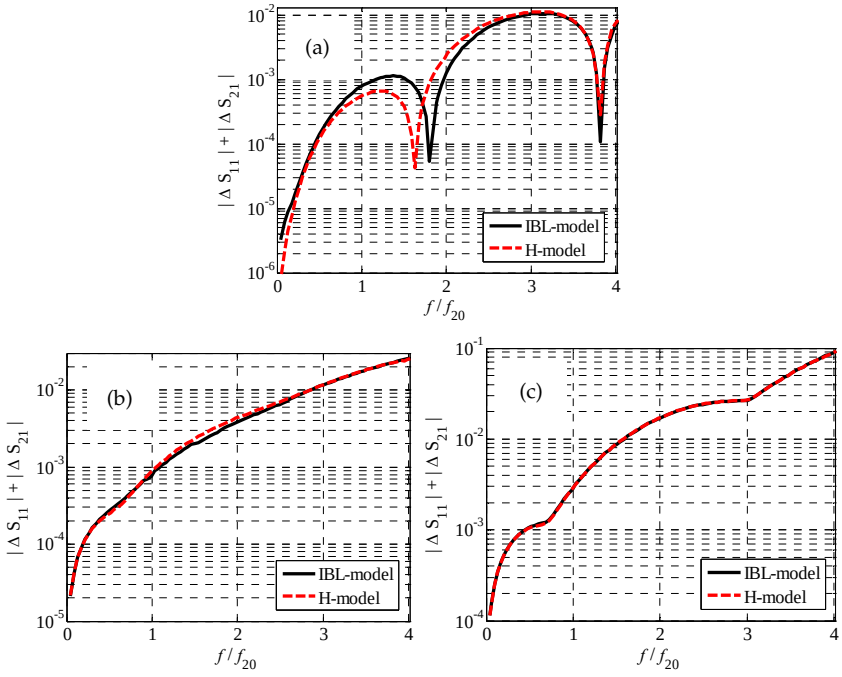

Figure 15 The S-parameter differences for the H- and the IBL-models with parameters retrieved at normal incidence for (a) $\theta_o = 0°$; (b) $\theta_o = 30°$; and (c) $\theta_o = 60°$.

For the IBL-model, we first use the 2-layer method (see subsection 3.2.4) and Eq. (29)–Eq. (35) to determine $\varepsilon_b(\theta_o=0°)$ and $\varepsilon_m(\theta_o=0°)$ under normal incidence (see Fig. 12 for retrieval results). Similarly to the H-model, the differences '$|\Delta S_{11}| + |\Delta S_{21}|$' are calculated for $\theta_o = 0°$, 30°, and 60°, and implemented into Fig. 15.

It is clear that the performances of both the H-model with $\varepsilon_{eff}(\theta_o=0°)$ and the IBL-model with $\varepsilon_b(\theta_o=0°)$ and $\varepsilon_m(\theta_o=0°)$ deteriorate with increasing θ_o, which implies the angle-dependence of the parameters of both models. Moreover for an arbitrary θ_o, the IBL-model with parameters retrieved at normal incidence fails to display any superiority over the H-model with $\varepsilon_{eff}(\theta_o=0°)$. Even for normal incidence these two models exhibit the same-level performance although the IBL-model seems physically more reasonable. These un-

expected phenomena, consistent with the results by the field averaging method in [P3], could result from the imprecision of the 2-layer method, and the compensation method aiming at restoring physically sound medium parameters at the cost of inaccurate reproduction of the S-parameters.

Therefore, the angle-dependent parameters are developed for both models. For the H-model, we applied Eq. (22) for different θ_0 to get $\varepsilon_{eff}(\theta_0)$; for the IBL-model, the 2-layer method and Eq. (29)–Eq. (35) are adopted to determine the angle-dependent $\varepsilon_b(\theta_0)$ and $\varepsilon_m(\theta_0)$. The results are visualized in Fig. 8 and Fig. 12, respectively. For both models, angular dispersion becomes gradually visible as the frequency increases. Moreover, the IBL-model is shown to be insufficient to describe the composite slab under oblique incidence, due to the unphysical low-frequency divergence, shown in Fig. 12.

4.2.2 A-model [P4]

A straightforward way to determine the parameters of the A-model is to compute the x- and y-components of the permittivity ε_x and ε_y by Eq. (28). The retrieval results, however, suffer severely from the FPRs and display unphysical behavior, as shown in Fig. 9. Then, we need another way to settle ε_x and ε_y. At normal incidence, the A-model will reduce to the H-model, leading to that ε_y equals $\varepsilon_{eff}(\theta_0=0°)$. Assuming that the model parameters are angle independent, ε_y will then be fixed as $\varepsilon_{eff}(\theta_0=0°)$, and ε_x can be calculated using Eq. (28) for different θ_0. Fig. 16 shows that the retrieved ε_x not only decreases as the frequency grows, but displays dependence on θ_0. Therefore, the angle dependence has to be introduced to both ε_x and ε_y.

As described in subsection 3.2.3, a closer examination on Eq. (22) and Eq. (28) reveals that ε_{eff} and ε_y are actually identical before the compensation, which makes it a good approximation to let $\varepsilon_y(\theta_0)$ equal to the compensated angle-dependent $\varepsilon_{eff}(\theta_0)$ of the H-model. We can then solve ε_x by Eq. (28). Fig. 9 visualizes the frequency-dependent ε_x and ε_y retrieved at different θ_0. At low frequencies, ε_x and ε_y curves converge to two different values, one of which (ε_y) is larger than the Lord Rayleigh estimate while the other (ε_x) is smaller. As the frequency grows, the angle dependence of ε_x and ε_y becomes more and more visible, indicating that the anisotropy cannot effectively describe spatial dispersion.

4.2.3 ABL-model

The first attempt is to determine the parameters of the ABL-model on the basis of the IBL-model, since under normal incidence these two models are equivalent. Similarly to Fig. 16, the retrieved ε_{bx} decreases with growing frequency and is dependent on the incident angle. Alternatively, we can fix ε_m of

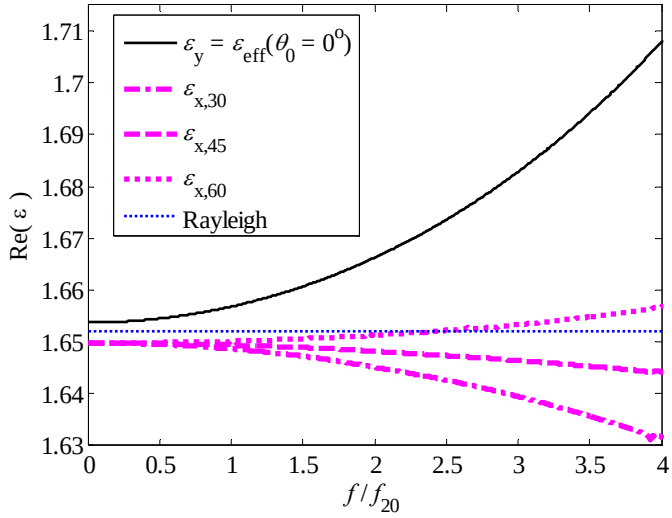

Figure 16 Retrieved ε_x of the A-model for various incident angles when ε_y is fixed as $\varepsilon_{eff}(\theta_o=0)$. The subscript x, y, numerals denote the *x*-direction, *y*-direction and the incident angles.

the ABL-model as $\varepsilon_m(\theta_o=0°)$ of the IBL-model, and then retrieve ε_{bx} and ε_{by} numerically for different θ_o. The retrieved results are, however, severely influenced by the FPRs.

As discussed in subsection 3.2.4, we can instead resolve ε_{bx} and ε_{by} at a certain θ_o by computing ε_x and ε_y of the A-model for a 2-layer slab at the same θ_o. Given the ε_{bx} and ε_{by} determined by the 2-layer method, we can then numerically solve $\varepsilon_m(\theta_o)$ using Eq. (29)–Eq. (35). The acquired permittivities are visualized in Fig. 13.

It is important to notice from Fig. 13 that due to the anisotropic boundary layers instead of the isotropic ones, all the retrieved ε_m curves converge and gradually approach the static Rayleigh estimate at low frequencies. The comparison between the retrieved ε_m for different θ_o in Figs. 12 and 13 shows that the separated boundary layers should be anisotropic, when the stratified homogenization model is applied to describe the composite slab of our interest under oblique incidence. Also, angular dispersion appears as the frequency grows. It is finally noted that angular dispersion in the ABL-model is slightly smaller than those of the H-model and the A-model.

4.2.4 Necessity of the additional boundary layers and the anisotropy

In order to assess the necessity of the anisotropy and the boundary layers, the MEP can be conducted at different θ_o for the three models (the H-, A-, and ABL-ones) with the derived angle-dependent parameters, as shown in Figs. 8,

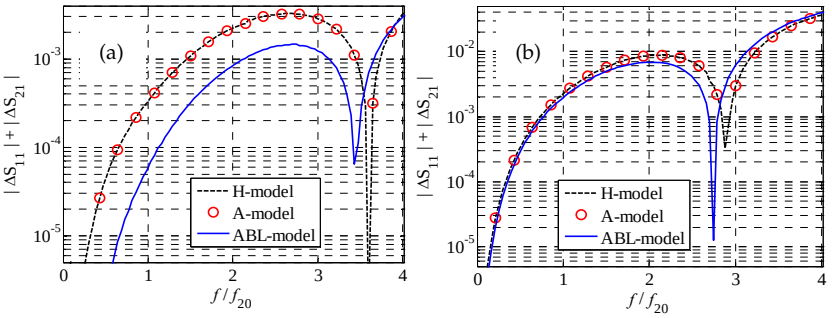

Figure 17 The S-parameter differences for the three proposed models with angle-dependent parameters. Dashed-black curve: H-model; red-circular markers: A-model; solid-blue curve: ABL-model. (a) $\theta_o = 30°$; (b) $\theta_o = 60°$.

9, and 13, respectively. The IBL-model is not taken into account since the retrieved angle-dependent model parameters exhibit an unreasonable behavior, i.e., the low frequency divergence of the retrieved ε_m shown in Fig. 12.

Several interesting phenomena can be observed in Fig. 17. Firstly, the comparison between the H- and the A-models with angle-dependent parameters shows that the anisotropy alone does not bring in any improvement. Therefore, it is clear that neither the isotropic boundary layer nor the anisotropy alone is sufficient to improve the model performance. However, the ABL-model clearly overwhelms the H- and A-models, which demonstrates that the boundary layers need to be anisotropic if the stratified homogenization model is applied.

Secondly, all these three models, despite angle-dependent parameters, produce larger errors with increasing θ_o. This phenomenon could arise from the finite number of the layers composing the slab in the x-direction. As θ_o increases, the electrical response in the x-direction will gradually dominate. However, only five layers of unit cells exist in this direction. This fact prevents the slab from being homogenized properly. The deterioration of the model performance could therefore be expected for a large θ_o.

Thirdly, the compensation method (Eq. (22)) aims at restoring physically sound dispersive permittivities for the dielectric slabs. Inevitably, it brings into the system some error measured by $|\Delta S_{11}|+|\Delta S_{21}|$. For instance, if the S-parameters are in turn calculated from the H- and the A-models with derived angle-dependent parameters, the errors will be included in z'. On the other hand, n' are not influenced, and they are identical for two models. From Eq. (23) and Eq. (24), it is found that $z' = n'(\varepsilon_{eff}\cos\theta_o)^{-1}$ for the H-model and $z' = n'(\varepsilon_y\cos\theta_o)^{-1}$ for the A-model. The z' are then identical since we assume $\varepsilon_y(\theta_o) = \varepsilon_{eff}(\theta_o)$. It can hence be expected that when equipped with angle-dependent parameters, the A-model and the H-model are of the same quality.

Finally, in spite of the extra complexities introduced into the H-model, an-

gular dispersion as the main obstacle to a proper homogenization is not obviously diminished. This pessimistic result indicates that it may be unnecessary to introduce more complicated models than the homogeneous one. This point could also be seen from Fig. 17 that for higher frequencies ($f/f_{20} > 3.5$) it is difficult to judge which model is superior to others. In addition, it may suggest that other complexities, such as magneto-electric effect, could be worth to investigate.

4.3 Transient waveform analysis in dispersive dielectric media [P6, P7]

Another important dispersion-modeling-based application is the analysis of temporal dynamics of electromagnetic pulses propagating in dispersive dielectric (composite) media. Most of time- or frequency-domain analyses aiming at this topic require a priori knowledge of the dispersion of the electrical properties of the media. In this subsection and [P6, P7], a straightforward frequency domain method is introduced. Based on this method, the transient waveform of a propagating pulse in a dielectric (composite) medium can be studied as long as the dispersion of the medium is known. In [P6], we studied temporal dynamics of different Gaussian pulses in dielectric (composite) media whose dispersions follow the Lorentz model (see Chapter 2). In [P7], dynamic evolution of Gaussian pulses inside aqueous mixtures (assumed to display the Debye-type dispersion) is discussed. Moreover, in this subsection, the presence of Sommerfeld precursor [71] and Brillouin precursor [72, 73] in dynamic evolution of a launched pulse is discussed when the dispersion of the medium is characterized by the Lorentz, the Debye, and the Fröhlich models, respectively.

The propagation of electromagnetic pulses in dispersive dielectric (composite) media can analytically be studied by the asymptotic method of steepest descent [74–80]. Numerically, this problem can be dealt with Fast Fourier Transform (FFT). For the initial temporal signal $f(t)$, its frequency spectrum $F(\omega)$ can be calculated by Fourier Transform. When the signal propagates in a medium, whose relative (effective) permittivity reads $\varepsilon(\omega)$, for a distance z, the propagated spectrum can be formulated as $F(\omega)\exp(-jk_1 z)$, where the effective wave number k_1 inside the medium is defined by $k_1^2 = \omega^2 c^{-2}\varepsilon$. By Inverse Fourier Transform, the transient waveform of the signal $f(t,z)$ can be determined. With the aid of FFT, the above algorithm can be readily implemented. Therefore, once the dispersion of the (effective) permittivity of the dielectric (composite) medium is modeled, the temporal pulse evolution inside it can be solved numerically. One may notice that in [P6, P7] a parameter θ (= ct/z) is widely applied instead of the time t to illustrate the transient

waveform of a launched pulse. This dimensionless parameter θ is more convenient to indicate the velocities of different components of a propagating pulse train [80]. For instance, Sommerfeld precursor should appear exactly at $\theta = 1$ since it propagates at c, i.e., speed of light in vacuum.

When the pulse penetrates deep into a dispersive dielectric medium, its dynamic evolution may be dominated by the precursor fields [81–84]. Besides the modulated waveform of the pulse, it is the high-frequency and the low-frequency absorptions of the medium that decide the presence of Sommerfeld precursor and Brillouin precursor in the dynamic evolution. Several characteristic parameters, defined to measure the absorption properties of the Lorentz, the Debye, and the Fröhlich models, are listed in Table 1.

Table 1 Values of characteristic parameters when $\omega \to +\infty$ and $\omega \to 0$.

	ω	$\varepsilon''(\omega)$	$\kappa(\omega)$	$k_I(\omega)$	*Sommerfeld*	*Brillouin*
Debye Model	$+\infty$	ω^{-1}	ω^{-1}	$(2\tau c)^{-1}(\varepsilon_\infty)^{-1/2}\Delta\varepsilon$	*No*	
	0	0	0	0		*Yes*
Lorentz Model	$+\infty$	ω^{-3}	ω^{-3}	ω^{-2}	*Yes*	
	0	0	0	0		*Yes*
Fröhlich Model	$+\infty$	ω^{-1}	ω^{-1}	$(2\tau c)^{-1}(\varepsilon_\infty)^{-1/2}\Delta\varepsilon$	*No*	
	0	0	0	0		*Yes*

In Table 1, $\varepsilon''(\omega)$ is the imaginary part of the relative permittivity, $\kappa(\omega)$ denotes the imaginary part of the refractive index, and $k_I(\omega)$ represents the imaginary part of the wavenumber. It is shown that the high frequency components of the input field suffer non-negligible attenuations in Debye-type and Fröhlich-type media, while Lorentz-type media is almost transparent for them. Therefore, the high frequency Sommerfeld precursor only appears when the pulse propagates in a medium with Lorentz-type dispersion. On the other hand, the low frequency Brillouin precursor can be observed in media with all the three types of dispersion. It should be mentioned that there is a physical inconsistency in the Debye model when it is applied to approximate the dispersive dielectric property of water. The Debye model predicts that water remains opaque at frequencies much higher than the relaxation frequency. This contradicts the simple fact that water is transparent in the visible range. Therefore, the Debye model overestimates the attenuation of water for frequencies much higher than the relaxation one. Caution should then be paid when one studies the presence of Sommerfeld precursor for a pulse penetrating into water using the Debye model.

Finally, Brillouin precursor is of practical importance since it decays alge-

braically instead of exponentially in a dissipative (composite) medium. One can take the aqueous mixture as an example. In [P7], they are modeled as the Debye raisin mixtures, and thus their dispersive effective permittivities could be approximated by the Maxwell Garnett mixing formula and the Debye model, as discussed in Chapter 2. The algebraic attenuation of the Brillouin precursor in the aqueous mixtures with modeled effective permittivities is then confirmed by the FFT. All the relevant results can be found in [P6, P7].

5. Summary of the publications

P1: Dispersion of the dielectric Fröhlich model and mixtures

The motivation behind this paper is the following. In order to accurately represent the permittivity of pure water over 0–25 THz and within 0–100°C, Ellison constructed an interpolation function by adding two resonance terms to the classical Debye model. These two terms represent two far-infrared molecular resonances of the water, and take the form of the Fröhlich model [85]. Unlike the Debye model and the Lorentz model, the Fröhlich one is not widely applied and its dispersion mechanism has not been clearly elucidated. Hence, this paper studies the distinctive dispersion mechanism, and that of the so-called Fröhlich raisin mixture based on the Maxwell Garnett mixing formula.

The dispersion of the Fröhlich model is shown to be a transition mechanism from the Debye-type relaxation process to the Lorentz-type resonance process when the characteristic parameters $\omega_0\tau$ increases from zero. In order to distinguish this process from the pure Debye and the pure Lorentz ones, the Fröhlich model is interpreted as a combination of a shifted passive Debye-type, a shifted active Debye-type and a Lorentz-type dispersions, i.e., Eq. (3) in [P1].

It is also shown based on the Maxwell Garnett mixing rule that the Fröhlich raisin mixture does not retain the same dispersion as its inclusions. Depending on the inclusion volume fraction, the dispersion mechanism may display the DDTD or the LDDD. The limiting volume fraction separating these two dispersion types is defined as f_b, which increases as the permittivity contrast $\varepsilon_i/\varepsilon_e$ grows. Admittedly, two issues limit the practical application of the results regarding the mixtures. Firstly, the volume fraction cannot to extremely large since the Mixing Garnett rule neglects the inclusion interactions. Secondly, to ensure the validity of the defined effective permittivity, we should stay close to the quasi-static limit, which may in turn considerably constrain the inclusion dimension if a strong dispersion is encountered.

P2: Quasi-dynamic homogenization of geometrically simple dielectric composites

This paper discusses the quasi-dynamic homogenization of dielectric composites when the electrical properties in particular directions are interested. Two types of composites with simple geometries are effectively treated as homogeneous media. Both composites contain the same unit cell made of a dielectric spherical inclusion centered in a dielectric cubic box. For the com-

posite with finite thickness, four retrieval methods based on the S-parameters are applied to resolve the dispersion of its transversal effective permittivity when the composite is illuminated by a normally incident plane wave. For the infinite simple cubic lattice, the dispersive effective permittivity is computed based on the dispersion diagram. Both the S-parameters and the dispersion diagram are generated in the full wave simulator CST MWS. It is shown that since the unit cell size does not strictly satisfy the long-wavelength restriction, the retrieval results from both S-parameters display unphysical behaviors. In order to effectively eliminate the broadband influence of the FPR as well as to restore physically reasonable medium parameters, a compensation method is introduced based on the nonmagnetic assumption. Also, the results by only S_{21} and by the EWM reveal similar dispersions as the compensated results, while the S_{11} method turns out to be unstable. On the other hand, by the dispersion diagram, the ε_{eff} of the lattice along the edge, the surface diagonal, and the volume diagonal of the unit cell are studied. The ε_{eff} along the unit cell edge is shown to agree well with the transversal ε_{eff} of the composite slab.

Based on the retrieved transversal ε_{eff}, the upper frequency limit f_L/f_{20} of the quasi-static estimate (the static Lord Rayleigh result ε_{Ray}) for the considered composites is defined by imposing a satisfactory tolerance, which reads $|\ \varepsilon_{\text{Ray}} - \varepsilon_{\text{Ray}}\ |\ /\ \varepsilon_{\text{Ray}} < 1\%$. However, the computational complexity of the 3D simulation prevents us from any exhaustive parametric analyses on f_L/f_{20} for different p and ε_i. Instead, a one-dimensional lattice is considered to cast a light to the dependence of f_L/f_{20} on p and ε_i.

P3: Homogenization of thin dielectric composite slabs: techniques and limitations

As the parallel work of [P2], the same composite slab with finite thickness as in [P2] is considered. Only the transversal effective permittivity is of interest. Two homogenization techniques, one from outside (S-parameter retrieval and homogeneous model) and the other one from inside (field averaging method and the boundary transition layer model), are compared when a plane wave is normally incident on the slab. It is demonstrated that the field averaging results agree well with those by the S-parameter retrieval and the compensation method. But both methods produce roughly the same level errors measured by the S-parameters.

In addition, the field averaging method leads to the following observations. Firstly, at low frequency, the effective permittivity ε_{eff} of the whole slab is slightly larger than the static Lord Rayleigh estimate ε_{Ray}, and grows with the increase of the frequency. Secondly, the more layers the slab contains, the closer ε_{eff} approaches ε_{Ray}. Thirdly, the outermost boundary layers display larger electrical response than all the other inner layers, whose permittivities are identical. Finally, the permittivities of the boundary layers and the inner

layers do not dramatically vary with the number of layers composing the slab. These results motivate us to apply the stratified model to describe the composites slab, and inspire the 2-layer method discussed in subsection 3.2.4. They also imply that enough number of layers is a necessary condition so that the slab could be treated as a homogeneous medium.

P4: Compensation of Fabry–Pérot resonances in homogenization of dielectric composites

This letter focuses on how to eliminate the broadband influence of the FPRs on the effective permittivities or its different components when lossless or low-loss composite slabs are homogenized as a homogeneous isotropic model or an anisotropic one. In addition, the retrieval methods based on S-parameters for both models, when a plane wave is obliquely incident on the slab, are derived. Two compensation methods are presented for different models, and are capable of restoring physically reasonable dispersion of the permittivities. The errors due to the compensation are then shown to increase with growing frequency, which restricts the applicable frequency range of the proposed compensation methods.

P5: Different homogenization methods based on scattering parameters of dielectric-composite slabs

This paper generalizes the results in [P2]. The dispersion of the effective permittivity of a 2D dielectric-composite slab is analyzed in a quasi-dynamic range using the simulated transmission and reflection data from the slab illuminated by an obliquely incident plane wave. The BSCM, the S_{11} method, the S_{21} method, and the EWM are generalized into oblique incidence. The BSCM turns out to be the most stable method, while the robustness of other methods depends on the incident angle of the illuminating plane wave.

Based on the retrieval results, the procedure for finding the dynamic trust region of the quasi-static Lord Rayleigh estimate for the effective permittivities of such composites is then developed. According to this process, the upper frequency limit f_L/f_{20} of this trust region is more rigorously defined, compared with [P2], by taking angular dispersion into account. The f_L/f_{20} is numerically determined by an interpolation function. The proposed function of the inclusion area fraction p and relative permittivity ε_i is demonstrated as a good predictor within the ranges $0.1 \le p \le 0.5$ and $10 \le \varepsilon_i \le 60$. It is further shown that within the above ranges the effective wavelength inside the material should be at least 33 times the edge length of the unit cell, in order to ensure that the defined relative difference between the retrieved effective permittivity and the quasi-static estimate is not larger than 1%.

P6: Truncation effect on precursor field structure of pulse propagation in dispersive media

In this paper, the dynamic evolutions of different Gaussian pulses in the dispersive Lorentz medium are analyzed by Fast Fourier Transform (FFT). The transient waveform of a full-Gaussian-modulated pulse for different penetration depth is first visualized. The decaying rates of different components of the pulse sequence are used to identify the precursors. It is shown that Sommerfeld precursor is absent in the temporal pulse dynamics, and that the Brillouin effect appears as a tail rather than a precursor.

Then, the truncated Gaussian pulses at different zero-crossing points are launched into the same Lorentz medium. It is shown that depending on the turn-on point, the Brillouin effect can be separated into a tail and a forerunner. In addition, an artificial Sommerfeld precursor due to the computation precision is pointed out.

P7: Evolution of the time-domain structure of electromagnetic pulse propagating in aqueous mixtures

The temporal dynamics of a Gaussian-modulated sinusoidal pulse in pure water and a class of conceivable aqueous mixtures is analyzed in this paper by FFT. The absence of Sommerfeld precursor in the dynamic pulse evolution is numerically demonstrated, and theoretically interpreted by the non-negligible high-frequency attenuation properties of the modeled materials. In addition, the algebraic decaying property of Brillouin precursor is numerically confirmed.

In this paper, Ellison's interpolation function [85] is applied to characterize the electric properties of pure water; and those of the aqueous mixtures are approximated by further employing Maxwell Garnett mixing formula. Based on the volume-fraction-dependent decaying property of the pulse propagating in aqueous mixtures, a method to detect water content of moisture substances is theoretically suggested.

References

[1] G. W. Milton, *The Theory of Composites*. Cambridge: Cambridge University Press, 2002.

[2] L. D. Landau, E. M. Lifshitz, and L. P. Pitaevskii, *Electrodynamics of Continu-ous Media, 2nd edition*. Burlington: Elsevier Butterworth–Heinemann, 1984.

[3] O. A. Oleinik, A. S. Shamaev, and G. A. Yosifian, *Mathematical Problems in Elasticity and Homogenization*. Amsterdam: Elsevier Science Publishers, 1991.

[4] W. S. Weiglhofer and A. Lakhtakia, *Introduction to Complex Mediums for Optics and Electromagnetics*. Bellingham, Washington: SPIE Press, 2003.

[5] J. D. Joannopoulos, R. D. Meade, and J. N. Winn, *Photonic Crystals*. New Jersey: Princeton University Press, 1995.

[6] C. Croënne, N. Fabre, D. P. Gaillot, O. Vanbésien, and D. Lippens, "Bloch impedance in negative index photonic crystals," *Physical Review B*, vol. 77, p. 125333, 2008.

[7] J. F. Galisteo-López, M. Galli, M. Patrini, A. Balestreri, L. C. Andreani, and C. López, "Effective refractive index and group velocity determination of three-dimensional photonic crystals by means of white light interferometry," *Physical Review B*, vol. 73, p. 125103, 2006.

[8] B. T. Schwartz and R. Piestun, "Dynamic properties of photonic crystals and their effective refractive index," *Journal of the Optical Society of American B*, vol. 22, pp. 2018–2026, 2005.

[9] M. Mojahedi and G. V. Eleftheriades, "Dispersion engineering: the use of abnormal velocities and negative index of refraction to control dispersive effects," in *Negative Refraction Metamaterials: Fundamental Properties and Applications*, New York: IEEE Press-Wiley Interscience, 2005.

[10] R. Magnusson, M. Shokooh-Saremi, and X. Wang, "Dispersion engineering with leaky-mode resonant photonic lattices," *Optics Express*, vol. 18, pp. 108–116, 2010.

[11] J. C. M. Garnett, "Colours in metal glasses and in metallic films," *Philosophical Transactions of the Royal Society of London*, vol. 203, pp. 385–420, 1904.

[12] V. G. Veselago, "The electrodynamics of substances with simultaneously negative values of ε and μ," *Soviet Physics Uspekhi*, vol. 10, pp. 509–514, 1968.

[13] J. Pendry, "Negative refraction," *Contemporary Physics*, vol. 45, pp. 191–202, 2004.

[14] R. A. Shelby, D. R. Smith, and S. Schultz, "Experimental verification of a negative index of refraction," *Science*, vol. 292, pp. 77–79, 2001.

[15] T. Koschny, P. Markoscaron, D. R. Smith, and C. M. Soukoulis, "Resonant and antiresonant frequency dependence of the effective parameters of

metamaterials," *Physical Review E*, vol. 68, p. 065602, 2003.

[16] R. A. Depine and A. Lakhtakia, "Comment I on "Resonant and antiresonant frequency dependence of the effective parameters of metamaterials"," *Physical Review E*, vol. 70, p. 048601, 2004.

[17] A. L. Efros, "Comment II on "Resonant and antiresonant frequency dependence of the effective parameters of metamaterials"," *Physical Review E*, vol. 70, p. 048602, 2004.

[18] T. Koschny, P. Markoscaron, D. R. Smith, and C. M. Soukoulis, "Reply to Comments on "Resonant and antiresonant frequency dependence of the effective parameters of metamaterials"," *Physical Review E*, vol. 70, p. 048603, 2004.

[19] T.-C. Yang, Y.-H. Yang, and T.-J. Yen, "An anisotropic negative refractive index medium operated at multiple-angle incidences," *Optics Express*, vol. 17, pp. 24189–24197, 2009.

[20] L. Rayleigh, "On the influence of obstacles arranged in rectangular order upon the properties of a medium," *Philosophical Magazine*, vol. 34, pp. 481–502, 1892.

[21] J. D. Jackson, *Classical Electrodynamics, 3rd Edition*. New York: John Wiley and Sons, Inc., 1999.

[22] B. K. P. Scaife, *Principles of Dielectrics*. Oxford: Oxford Science Publications, 1989.

[23] B. M. Kolundzija and A. R. Djordjevic, *Electromagnetic Modeling of Composite Metallic and Dielectric Structures*. Norwood, Massachusetts: Artech House, 2002.

[24] A. V. Hippel, *Dielectric Materials and Applications*. Boston: Artech House, 1995.

[25] F. Kremer and A. Schönhals, *Broadband Dielectric Spectroscopy*. Verlag Berlin Heidelberg: Springer, 2002.

[26] P. J. W. Debye, *The Collected Papers of Peter J. W. Debye*. New York: Interscience, 1954.

[27] H. A. Lorentz, *The Theory of Electrons and Its Applications to the Phenomena of Light and Radiant Heat*. Leipzig, Germany: Teubner, 1909.

[28] H. Fröhlich, *Theory of Dielectrics: Dielectric Constant and Dielectric Loss*. Oxford: Oxford Science Publications, 1987.

[29] A. Sihvola, *Electromagnetic Mixing Formulas and Applications*. London: IEE, 1999.

[30] K. Oughstun and N. Cartwright, "On the Lorentz–Lorenz formula and the Lorentz model of dielectric dispersion," *Optics Express*, vol. 11, pp. 1541–1546, 2003.

[31] J. H. V. Vleck and V. F. Weisskopf, "On the shape of collision-broadened lines," *Reviews of Modern Physic*s, vol. 17, pp. 227–236, 1945.

[32] O. F. Mossotti, "Discussione analitica sull'influenza che l'azione di un mezzo dielettrico ha sulla distribuzione dell'elettricità alla superficie di più corpi elettrici disseminati in esso," *Memorie di Mathematica e di Fisica della Società Italiana della Scienza Residente in Modena*, vol. 24, pp. 49–74, 1850.

[33] R. Clausius, *Abhandlungen über die Mechanische Wärmetheorie*. Braunschweig: Friedrich Vieweg und Sohn, 1864.

[34] J. Qi, H. Kettunen, H. Wallén, and A. Sihvola, "Different retrieval methods

based on S-parameters for the permittivity of composites," in *Electromagnetic Theory (EMTS), 2010 URSI International Symposium on*, pp. 588–591.

[35] A. Kraszewski, *Microwave Aquametry*. New York: IEEE Press, 1996.

[36] K. Kärkkäinen, A. Sihvola, and K. Nikoskinen, "Analysis of a three-dimensional dielectric mixture with finite difference method," *IEEE Transactions on Geoscience and Remote Sensing*, vol. 39, pp. 1013–1018, 2001.

[37] M. Avellaneda, "Iterated homogenization differential effective medium theory and applications," *Communications On Pure and Applied Mathematics*, vol. 40, pp. 527–554, 1987.

[38] R. Diaz, W. Merrill, and N. Alexopoulos, "Analytic framework for the modeling of effective media," *Journal of Applied Physics*, vol. 84, pp. 6815–6826, 1998.

[39] C. Brosseau, "Modelling and simulation of dielectric heterostructures: a physical survey from an historical perspective," *Journal of Physics D-Applied Physics*, vol. 39, pp. 1277–1294, 2006.

[40] F. Seitz, *The Modern Theory of Solids*. New York: McGraw–Hill, 1940.

[41] C. S. T. AG, *CST Microwave Studio 2009*, www.cst.com, 2009.

[42] Comsol, *Comsol Multiphysics 3.5*, www.comsol.com, 2010.

[43] H. Kettunen, J. Qi, H. Wallén, and A. Sihvola, "Homogenization of dielectric composites with finite thickness," in *the 26th Annual Review of Progress in Applied Computational Electromagnetics*, Tampere, Finland, 2010, pp. 490–495.

[44] H. Wallén, H. Kettunen, J. Qi, and A. Sihvola, "A geometrically simple benchmark problem for negative index metamaterial homogenization," in *Electromagnetic Theory (EMTS), 2010 URSI International Symposium on*, pp. 768–771.

[45] A. M. Nicolson and G. F. Ross, "Measurement of the intrinsic properties of materials by time-domain techniques," *IEEE Transsactions on Instrumentation and Measurement*, vol. IM–19, pp. 377–382, 1970.

[46] W. B. Weir, "Automatic measurement of complex dielectric-constant and permeability at microwave-frequencies," *Proceedings of the IEEE*, vol. 62, pp. 33–36, 1974.

[47] R. W. Ziolkowski, "Design, fabrication, and testing of double negative metamaterials," *IEEE Transactions on Antennas and Propagation*, vol. 51, pp. 1516–1529, 2003.

[48] S. Zouhdi, A. Sihvola, and A. P. Vinogradov, *Metamaterials and Plasmonics: Fundamentals, Modelling, Applications*. New York: Springer–Verlag, 2008.

[49] C. R. Simovski, "Material parameters of metamaterials," *Optics and Spectroscopy*, vol. 107, pp. 726–753, 2009.

[50] D. R. Smith, S. Schultz, P. Markoš, and C. M. Soukoulis, "Determination of effective permittivity and permeability of metamaterials from reflection and transmission coefficients," *Physical Review B*, vol. 65, p. 195104, 2002.

[51] X. Chen, B. I. Wu, J. A. Kong, and T. M. Grzegorczyk, "Retrieval of the effective constitutive parameters of bianisotropic metamaterials," *Physical Review E*, vol. 71, p. 046610, 2005.

[52] Z. F. Li, K. Aydin, and E. Ozbay, "Determination of the effective constitutive

parameters of bianisotropic metamaterials from reflection and transmission coefficients," *Physical Review E*, vol. 79, p. 026610, 2009.

[53] B. N. Wang, J. F. Zhou, T. Koschny, M. Kafesaki, and C. M. Soukoulis, "Chiral metamaterials: simulations and experiments," *Journal of Optics A-Pure and Applied Optics*, vol. 11, p. 114003, 2009.

[54] X. Chen, T. M. Grzegorczyk, B.-I. Wu, J. Pacheco, and J. A. Kong, "Robust method to retrieve the constitutive effective parameters of metamaterials," *Physical Review E*, vol. 70, p. 016608, 2004.

[55] D. Sjöberg and C. Larsson, "Characterization of composite materials in waveguides," in *Electromagnetic Theory (EMTS), 2010 URSI International Symposium on*, pp. 592–595.

[56] J. Baker-Jarvis, E. J. Vanzura, and W. A. Kissick, "Improved technique for determining complex permittivity with the transmission/reflection method," *IEEE Transactions on Microwave Theory and Techniques*, vol. 38, pp. 1096–1103, 1990.

[57] K. Levenberg, "A method for the solution of certain non-linear problems in least squares," *Quarterly of Applied Mathematics*, pp. 164–168, 1944.

[58] J. Qi, H. Kettunen, H. Wallén, and A. Sihvola, "Homogenization model evaluation for a dielectric-composite slab upon oblique incidence," Unpublished manuscript.

[59] G. Mahan and G. Obermair, "Polaritons at surfaces," *Physical Review*, vol. 183, pp. 834–841, 1969.

[60] C. R. Simovski, S. A. Tretyakov, A. H. Sihvola, and M. M. Popov, "On the surface effect in thin molecular or composite layers," *European Physical Journal-Applied Physics*, vol. 9, pp. 195–204, 2000.

[61] J. A. Kong, *Electromagnetic Wave Theory*. Cambridge, USA: EMW Publishing, 2008.

[62] D. R. Smith and J. B. Pendry, "Homogenization of metamaterials by field averaging (invited paper)," *Journal of the Optical Society of America B–Optical Physics*, vol. 23, pp. 391–403, 2006.

[63] C. Fietz and G. Shvets, "Current-driven metamaterial homogenization," *Physica B–Condensed Matter*, vol. 405, pp. 2930–2934, 2010.

[64] M. G. Silveirinha, "Metamaterial homogenization approach with application to the characterization of microstructured composites with negative parameters," *Physical Review B*, vol. 75, p. 115104, 2007.

[65] C. R. Simovski and P. A. Belov, "Low-frequency spatial dispersion in wire media," *Physical Review,* vol. 70, p. 046616, 2004.

[66] C. R. Simovski and S. A. Tretyakov, "Local constitutive parameters of metamaterials from an effective-medium perspective," *Physical Review B,* vol. 75, p. 195111, 2007.

[67] M. G. Silveirinha and C. A. Fernandes, "Homogenization of 3-D-connected and nonconnected wire metamaterials," *IEEE Transactions on Microwave Theory and Techniques*, vol. 53, pp. 1418–1430, 2005.

[68] C. R. Simovski, "On electromagnetic characterization and homogenization of nanostructured metamaterials," *Journal of Optics,* vol. 13, p. 013001, 2011.

[69] R. C. McPhedran, C. G. Poulton, N. A. Nicorovici, and A. B. Movchan, "Low frequency corrections to the static effective dielectric constant of a two-dimensional composite material," *Proceedings of the Royal Society of*

London Series A–Mathematical Physical and Engineering Sciences, vol. 452, pp. 2231–2245, 1996.

[70] MathWorks, *Matlab 2009b*, www.mathworks.com/products/matlab, 2009.

[71] A. Sommerfeld, "Über die Fortpflanzung des Lichtes in dispergierenden Medien," *Annals of Physics*, vol. 44, pp. 177–202, 1914.

[72] L. Brillouin, "Über die Fortpflanzung des Licht in dispergierenden Medien," *Annals of Physics*, vol. 44, pp. 203–240, 1914.

[73] L. Brillouin, *Wave Propagation and Group Velocity*. New York: Academic Press, 1964.

[74] K. E. Oughstun and G. C. Sherman, "Propagation of electromagnetic pulses in a linear dispersive medium with absorption (the Lorentz medium)," *Journal of the Optical Society of American B*, vol. 5, pp. 817–849, 1988.

[75] R. Albanese, J. Penn, and R. Medina, "Short-rise-time microwave pulse propagation through dispersive biological media," *Journal of the Optical Society of American A*, vol. 6, pp. 1441–1446, 1989.

[76] A. Sihvola, "Dielectric mixture theories in permittivity prediction: effect of water on the macroscopic parameters," in *Microwave Aquametry: Electromagnetic Wave Interaction with Water-Containing Materials*, A. Kraszewski, Ed.. New York: IEEE Press, 1996.

[77] P. Wyns, D. P. Foty, and K. E. Oughstun, "Numerical analysis of the precursor fields in linear dispersive pulse propagation," *Journal of the Optical Society of American A*, vol. 6, pp. 1421–1429, 1989.

[78] R. W. Ziolkowski and J. B. Judkins, "Propagation characteristics of ultrawide-bandwidth pulsed Gaussian beams," *Journal of the Optical Society of American A*, vol. 9, pp. 2021–2030, 1992.

[79] C. M. Balictsis and K. E. Oughstun, "Uniform asymptotic description of ultrashort Gaussian-pulse propagation in a causal, dispersive dielectric," *Physical Review E*, vol. 47, pp. 3645–3669, 1993.

[80] K. E. Oughstun and C. M. Balictsis, "Gaussian pulse propagation in a dispersive, absorbing dielectric," *Physical Review Letters*, vol. 77, p. 2210, 1996.

[81] C. M. Balictsis and K. E. Oughstun, "Generalized asymptotic description of the propagated field dynamics in Gaussian pulse propagation in a linear, causally dispersive medium," *Physical Review E*, vol. 55, pp. 1910–1921, 1997.

[82] S. L. Dvorak, R. W. Ziolkowski, and L. B. Felsen, "Hybrid analytical-numerical approach for modeling transient wave propagation in Lorentz media," *Journal of the Optical Society of American A*, vol. 15, pp. 1241–1255, 1998.

[83] X. Ni and R. R. Alfano, "Brillouin precursor propagation in the THz region in Lorentz media," *Optics Express*, vol. 14, pp. 4188–4194, 2006.

[84] K. E. Oughstun, "Dynamical evolution of the Brillouin precursor in Rocard-Powles-Debye model dielectrics," *IEEE Transactions on Antennas and Propagation*, vol. 53, pp. 1582–1590, 2005.

[85] W. J. Ellison, "Permittivity of pure water, at standard atmospheric pressure, over the frequency range 0–25 THz and the temperature range 0–100 °C," *Journal of Physical and Chemical Reference Data*, vol. 36, pp. 1–18, 2007.

Errata

In [P1], Eq. (8) should read

$$\omega_0 \tau_b = \frac{\varepsilon_s - \varepsilon_\infty}{2\sqrt{(\varepsilon_\infty + 2\varepsilon_e)(\varepsilon_s + 2\varepsilon_e)}}. \tag{43}$$

Aalto-DD 61/2011

ISBN 978-952-60-4211-4 (pdf)
ISBN 978-952-60-4210-7
ISSN-L 1799-4934
ISSN 1799-4942 (pdf)
ISSN 1799-4934

Aalto University
School of Electrical Engineering
Department of Radio Science and Engineering
www.aalto.fi

BUSINESS + ECONOMY

ART + DESIGN + ARCHITECTURE

SCIENCE + TECHNOLOGY

CROSSOVER

DOCTORAL DISSERTATIONS